

InSight Pressure Data Recalibration, and its Application to the Study of Long-Term Pressure Changes on Mars

Lucas Lange^{1,1}, Francois Forget^{2,2}, Donald Banfield^{3,3}, Michael J. Wolff^{4,4}, Aymeric Spiga^{5,5}, Ehouarn Millour^{5,5}, Daniel Viúdez-Moreiras^{6,6}, Antoine Bierjon^{5,5}, Sylvain Piqueux^{7,7}, Claire Newman^{8,8}, Jorge Pla-García^{9,9}, and William Bruce Banerdt^{7,7}

¹Laboratoire de Météorologie Dynamique, Institut Pierre-Simon Laplace (LMD/IPSL), Sorbonne Université, Centre National de la Recherche Scientifique (CNRS), École Polytechnique, École Normale Supérieure (ENS), Paris, France

²Laboratoire de Meteorologie Dynamique

³Cornell

⁴Space Science Institute

⁵Laboratoire de Météorologie Dynamique

⁶Centro de Astrobiología (INTA-CSIC)

⁷Jet Propulsion Laboratory

⁸Aeolis Research

⁹Centro de Astrobiología (CSIC-INTA)

November 30, 2022

Abstract

Observations of the South Polar Residual Cap suggest a possible erosion of the cap, leading to an increase of the global mass of the atmosphere. We test this assumption by making the first comparison between Viking 1 and InSight surface pressure data that have been recorded with ~ 40 years of difference. Such a comparison also allows us to determine changes in the dynamics of the seasonal ice caps between these two periods. To do so, we first had to recalibrate the InSight pressure data because of their unexpected sensitivity to the sensor temperature. Then, we had to design a procedure to compare distant pressure measurements. We propose two surface pressure interpolation methods at the local and global scale to do the comparison. The comparison of Viking and InSight seasonal surface pressure variations does not show major changes in the CO_2 cycle. Such conclusions are also supported by an analysis of the Mars Science Laboratory (MSL) pressure data. Further comparisons with images of the south seasonal cap taken by the Viking 2 orbiter and MARCI camera do not display significant changes in the dynamic of this cap within ~ 40 years. Only a possible larger extension of the North Cap after the global storm of MY 34 is observed, but the physical mechanisms behind this anomaly are not well determined. Finally, the first comparison of MSL and InSight pressure data suggests a pressure deficit at Gale crater during southern summer, possibly resulting from a large presence of dust suspended within the crater.

1 **InSight Pressure Data Recalibration, and its Application**
2 **to the Study of Long-Term Pressure Changes on Mars**

3 **L.Lange¹, F.Forget¹, D.Banfield², M.Wolff³, A.Spiga^{1,4}, E.Millour¹, D.**
4 **Viúdez-Moreiras⁵, A.Bierjon¹, S.Piqueux⁶, C.Newman⁷, J.Pla-García^{5,8},**
5 **W.B.Banerdt⁶**

6 ¹Laboratoire de Météorologie Dynamique, Institut Pierre-Simon Laplace (LMD/IPSL), Sorbonne
7 Université, Centre National de la Recherche Scientifique (CNRS), École Polytechnique, École Normale
8 Supérieure (ENS), Paris, France

9 ²Cornell Center for Astrophysics and Planetary Science, Cornell University, Ithaca, NY, USA

10 ³Space Science Institute, Boulder, CO, USA

11 ⁴Institut Universitaire de France, Paris, France

12 ⁵Centro de Astrobiología (CSIC-INTA) and National Institute for Aerospace Technology (INTA), Madrid,
13 Spain

14 ⁶Jet Propulsion Laboratory, California Institute of Technology, Pasadena, CA 91109, USA

15 ⁷Aeolis Research, Unit 5, Chandler, AZ, USA

16 ⁸Southwest Research Institute, Boulder, CO, USA

17 **Key Points:**

- 18 • We propose a recalibration of InSight pressure data to correct an unexpected sen-
19 sitivity to the sensor temperature;
- 20 • A comparison between the InSight and Viking 1 pressure data does not show sec-
21 ular changes in the global mass of the atmosphere;
- 22 • This comparison also supports the absence of long-term variability in the dynam-
23 ics of seasonal cap formation and sublimation.

Corresponding author: Lucas Lange, lucas.lange@lmd.ipsl.fr

24 Abstract

25 Observations of the South Polar Residual Cap suggest a possible erosion of the cap,
26 leading to an increase of the global mass of the atmosphere. We test this assumption by
27 making the first comparison between Viking 1 and InSight surface pressure data, which
28 were recorded 40 years apart. Such a comparison also allows us to determine changes
29 in the dynamics of the seasonal ice caps between these two periods. To do so, we first
30 had to recalibrate the InSight pressure data because of their unexpected sensitivity to
31 the sensor temperature. Then, we had to design a procedure to compare distant pressure
32 measurements. We propose two surface pressure interpolation methods at the local
33 and global scale to do the comparison. The comparison of Viking and InSight seasonal
34 surface pressure variations does not show major changes in the CO₂ cycle. Such
35 conclusions are also supported by an analysis of Mars Science Laboratory (MSL) pressure
36 data. Further comparisons with images of the south seasonal cap taken by the Viking
37 2 orbiter and MARCI camera do not display significant changes in the dynamics of this
38 cap over a 40 year period. Only a possible larger extension of the North Cap after the
39 global storm of MY 34 is observed, but the physical mechanisms behind this anomaly
40 are not well determined. Finally, the first comparison of MSL and InSight pressure data
41 suggests a pressure deficit at Gale crater during southern summer, possibly resulting from
42 a large presence of dust suspended within the crater.

43 Plain Language Summary

44 Observations of the permanent CO₂ ice cap at the south pole of Mars in the 2000s
45 suggested that the cap was eroding, possibly releasing a significant amount of CO₂ into
46 the atmosphere. To test this hypothesis, we compare surface pressures recorded by Viking
47 in the 1970s and those recorded by InSight in 2018-2021 to confirm or refute the suspected
48 increase of the atmospheric mass. After establishing our comparison method, we correct
49 the influence of the sensor temperature on the InSight pressure data, which was discovered
50 during our investigation. Comparison of the pressure data, as well as images of the
51 seasonal caps taken by orbiters, do not reveal any change in the atmospheric mass or the
52 dynamics of the seasonal ice caps that develop during the martian year. These conclusions
53 are reinforced by reanalyzing the pressure data recorded by the Curiosity rover.
54 Only small interannual changes are observed, potentially related to the effect of the dust
55 storms that happened on Mars between 2016 and 2018. Finally, we report a possible pressure
56 deficit at MSL's location during southern hemisphere summer, potentially explained
57 by the unusual presence of dust in the crater air.

58 1 Introduction

59 The retreat of the Southern Seasonal Polar Cap (SSPC) during local summer leaves
60 a residual perennial deposit mainly composed of CO₂ ice (Kieffer et al., 1972). This deposit,
61 known as the South Polar Residual Cap (SPRC) can persist during the Southern
62 summer because of its high albedo (Jakosky & Haberle, 1990) and the exchanges with
63 the CO₂ ice at the surface and the CO₂ ice deposits that are buried at this location through
64 permeable water ice layers (Buhler et al., 2020). The SPRC is one of the CO₂ reservoirs
65 that can significantly affect the atmospheric mass through sublimation or deposition (Leighton
66 & Murray, 1966). The stability of this reservoir over time is a long-standing debate in
67 martian climate science. While Blackburn et al. (2010) predicted the disappearance of
68 the SPRC within a few years, Piqueux and Christensen (2008) reported limited changes
69 in the extent and ice-covered area of the SPRC since the Mariner 9 mission in 1972 and
70 telescopic observations in the twentieth century. However, Piqueux and Christensen (2008)
71 were unable to retrieve a mass balance of the cap. Other monitoring of the SPRC surface
72 since the Mariner 9 and Viking era led to mass balance estimates suggesting either
73 an erosion of the SPRC (Malin et al., 2001; Thomas et al., 2009; Blackburn et al., 2010;

74 Thomas et al., 2013, 2016) or a possible ice accretion (Thomas et al., 2016). This pre-
75 sumed erosion or accretion of the SPRC open the possibility of secular pressure changes
76 on Mars: if the SPRC loses CO₂ ice year after year, the sublimated CO₂ ice goes into
77 the atmosphere, increasing its global mass and thus also the global mean surface pres-
78 sure on Mars (Malin et al., 2001; Kahre & Haberle, 2010; Haberle & Kahre, 2010; Thomas
79 et al., 2016). Conversely, the deposition of CO₂ ice on the cap would decrease the at-
80 mospheric mass, and thus the atmospheric pressure. Observations from Malin et al. (2001)
81 suggested that the CO₂ ice thickness decreases by nearly 0.4 m per Martian Year (MY).
82 After computing the total volume of ice that is eroding, and assuming a CO₂ ice den-
83 sity of $1.6 \cdot 10^3 \text{ kg m}^{-3}$, they estimated that the amount of CO₂ released into the atmo-
84 sphere, and thus the increase of surface pressure, is nearly +13 Pa per Martian Decade
85 (MD). Blackburn et al. (2010) also estimated a possible increase of surface pressure be-
86 tween +0.5 and +13 Pa/MD. A recent study by Thomas et al. (2016) qualified the two
87 previous estimations by reporting a much smaller variation of SPRC mass balance, with
88 a possible variation of surface pressure between -2.3 Pa/MD and +1.6 Pa/MD.

89 In addition to this possible secular change in atmospheric mass, we can investigate
90 the possibility of an unknown mechanism that would change the dynamics of formation
91 and sublimation of the CO₂ seasonal caps. Thermal infrared observations (e.g., (Piqueux
92 et al., 2015)), spectroscopic studies (e.g., (Langevin et al., 2007; Brown et al., 2010)),
93 or cap albedo monitoring (e.g. (Calvin et al., 2015, 2017)) have already reported inter-
94 annual variability in the formation and recessions of the seasonal caps. However, no com-
95 parison has been made with the present observations (i.e., for martian year 35-36).

96 A direct way to assess long-term pressure changes on Mars consists of comparing
97 surface pressure measurements separated by several martian decades. By this method,
98 we can check if the atmospheric mass has changed, and study possible variability in the
99 dynamic of the seasonal ice caps. Such a comparison must be done carefully, however,
100 because of the influence of orography and meteorological variability on the annual sur-
101 face pressure cycle (Hourdin et al., 1993, 1995). The comparison of pressure measure-
102 ments made by Viking between 1976 and 1982 and those by Phoenix in 1997, after be-
103 ing corrected for both topography differences and atmospheric dynamics simulated by
104 a Global Circulation Model (GCM), showed a possible 10 Pa rise of surface pressure (Haberle
105 & Kahre, 2010) which corresponds to 5 Pa/MD. However, the combined uncertainties
106 in both the measurements and the interpolation methodology were not sufficiently ac-
107 curate to draw any conclusions about a secular pressure change. More recently, the com-
108 parison between Mars Science Laboratory pressure measurements, which have been recorded
109 since 2012, and Viking measurements did not show significant changes in surface pres-
110 sure (Haberle et al., 2014). However, these conclusions are limited by the sensitivity to
111 the hydrostatic adjustment of surface pressure as the rover is climbing Mount Sharp in
112 Gale Crater (Haberle et al., 2014; Richardson & Newman, 2018), and the sensitivity of
113 the atmospheric dynamics at Gale Crater that have to be resolved by a mesoscale model
114 (Pla-Garcia et al., 2016; Rafkin et al., 2016). Hence, the analysis of the first available
115 surface pressure data neither confirmed nor denied any long-term pressure changes. Re-
116 mote sensing measurements of surface pressure could be interesting to exploit (e.g., (Forget
117 et al., 2007; Withers, 2012)) but these measurements are not accurate enough compared
118 to in-situ surface pressure measurements and will not be exploited here.

119 In 2018, the InSight mission deployed a geophysical and meteorological observa-
120 tory, including a pressure sensor, at the surface of Mars (Banfield et al., 2019; Banerdt
121 et al., 2020). The instruments are deployed on a static lander at Elysium Planitia, a re-
122 latively flat area located at 4.5° N, 135.6° E (Golombek et al., 2020), thus reducing the
123 sensitivity of surface pressure measurements to both hydrostatic adjustment and atmo-
124 spheric dynamics. Pre-flight calibration and tests suggested that the performances of the
125 sensor were good enough to detect changes in the atmospheric mass and CO₂ cycle (Spiga
126 et al., 2018). We thus propose in this paper to compare the InSight pressure data with

127 the Viking pressure data to assess the possibility of long-term pressure changes over two
128 martian decades.

129 We present in section 2 the methodology of the pressure interpolation that will lead
130 our comparison between Viking and InSight data. A closer look at the InSight data re-
131 veals a calibration problem due to a sensor temperature sensitivity. We propose an em-
132 pirical recalibration and test the reliability of this correction in section 3. The compar-
133 ison between the InSight corrected pressure data and Viking surface pressure measure-
134 ments is then presented in section 4 to check for a possible secular increase or decrease
135 of atmospheric mass. Long-term variations in the dynamics of the seasonal ice caps be-
136 tween the 1970s and 2018 are also investigated using pressure data and satellite images
137 from the Viking and InSight eras, respectively. We then extend the scope of this study
138 by also exploiting the Phoenix and MSL measurements to detect any evolution of the
139 atmospheric mass in section 5. We also look at the possible influence of interannual vari-
140 ability of the seasonal cap due to the dust cycle. The main conclusions from our inves-
141 tigation are presented in section 6.

142 2 Methodology of Pressure Interpolation

143 The interpolation of the Viking pressure to the InSight landing site requires tak-
144 ing into account planetary-scale atmospheric dynamics that affect the surface pressure
145 (Hourdin et al., 1993, 1995). Even local interpolation between two close points must in-
146 clude the influence of local weather phenomena, like slope winds. Hence, interpolating
147 pressure cannot be limited to integrating the hydrostatic equation to correct for altitude
148 differences. To take into account the impact of atmospheric dynamics at all scales, we
149 propose two high-accuracy interpolation methods: one on a local scale (typically within
150 a crater, a slope, etc.), and one on a regional-to-global scale.

151 2.1 Local pressure interpolation

152 We consider here a local situation in which two points are close enough so that large-
153 scale dynamic pressure gradients related to the global atmospheric circulation and re-
154 gional flows can be neglected. Let us consider two points A and B located at different
155 altitudes (Figure 1a). Since these two points are close, the main factor that impacts the
156 difference in the absolute pressure is altitude, thus we could assume hydrostatic equi-
157 librium and recast pressure (P_B) at point B to the altitude at point A ($P_{B \rightarrow A}$) with:

$$P_{B \rightarrow A} = P_B e^{-\frac{z_A - z_B}{H}} \quad (1)$$

158 where z corresponds to the altitude of each point, H is the scale height expressed
159 as:

$$H = \frac{RT}{\mu g} \quad (2)$$

160 with $R = 8.3145 \text{ J kg}^{-1} \text{ mol}^{-1}$ the molar gas constant, T is the mean atmospheric tem-
161 perature between A and B weighted by vertical pressure field (in Kelvin), $\mu = 43.34 \times$
162 $10^{-3} \text{ kg mol}^{-1}$ the mean molecular weight of Mars atmosphere and $g = 3.72 \text{ m s}^{-2}$ Mars'
163 surface gravity.

164 On terrains with an uneven topography, local circulations, like slope winds, can ap-
165 pear as a consequence of temperature gradients. Hence, the choice of a scale height H ,
166 and thus the temperature to take into account in Eq. 2, is important to consider the ma-
167 jor effect of these local circulations (Spiga et al., 2007; Forget et al., 2007): the tem-
168 perature choice in H will indicate which path should be used to integrate the hydrostatic

169 equation (red and green lines in Figure 1a). Such effects are very important for the Mars
 170 Science Laboratory mission for instance. As the Curiosity rover moves in Gale Crater,
 171 with significant gains of elevation (several hundred meters), local circulations and slope
 172 winds (Pla-Garcia et al., 2016; Raffin et al., 2016; Richardson & Newman, 2018) also
 173 contribute to the absolute pressure recorded by the rover. Forget et al. (2007); Spiga et
 174 al. (2007) suggested using the temperature at an altitude of 1 km above the surface in
 175 Eq. 2 to take into account the effect of slope winds at the GCM scale, while Ordonez-
 176 Etxeberria et al. (2019) used the air temperature at an altitude of 2 m when using MSL
 177 pressure data. Haberle et al. (2014) also questioned the choice of the scale height H that
 178 has to be used when exploiting MSL data. Their study of the sensitivity of pressure data
 179 to this scale height shows that, with extreme temperature scenarios, the absolute pres-
 180 sure can be influenced by several Pascals. However, they never determine which scale
 181 height is the right one to use with these data.

182 Thus, we investigate here the scale height that better matches MSL observations,
 183 and quantify the errors made during the interpolation of the surface pressure, using the
 184 example of Gale Crater. To do so, simulations of Gale Crater with the LMD mesoscale
 185 model (Spiga & Forget, 2009) were performed. The domain for the simulations ranges
 186 from 22° S to 30° N and 108° E to 163° E, with a spatial resolution of 0.16° , including
 187 thus the InSight landing site, Gale Crater and its circulation.

188 We take the diurnal cycle of surface pressure simulated at several seasons at grid
 189 points at the bottom (B) and the rim of Gale Crater (A) ($\Delta z = 1725\text{m}$, in the axis of
 190 MSL trajectory). We then interpolate the pressure at point B (P_B) to location A using
 191 several altitudes for the temperature above the point B to compute H . We then com-
 192 pute the relative error between the exact modeled pressure at A (P_A), and the interpo-
 193 lated pressure from B to A ($P_{B \rightarrow A}$). Results are presented in Figure 1b. They show that
 194 choosing the temperature at an altitude between 500 m and 2 km above the surface is
 195 better to take into account the effect of local dynamics on the pressure interpolation as
 196 it minimizes the relative difference between P_A and $P_{B \rightarrow A}$. In the following, we choose
 197 to compute the scale height H by using the temperature at an altitude of 1 km. When
 198 interpolating actual measurements, this temperature is not available from observations
 199 and instead has to be estimated using an atmospheric model. The main uncertainty in
 200 this calculation results from the sensitivity of temperatures to the dust opacity, which
 201 is not perfectly known. To check the sensitivity of the interpolation to these weather con-
 202 ditions and thus to an error in T , we use the GCM runs to quantify the impact of the
 203 dust opacity using three dust scenarios as input:

- 204 • A climatology (*clim*) scenario, derived by averaging the available observations of
 205 dust from MY 24, 25, 26, 28, 29, 30, and 31 outside the global dust storm period
 206 (Montabone et al., 2015). This scenario represents a nominal dust scenario in the
 207 absence of major dust storms.
- 208 • A *cold* scenario which corresponds to an extremely clear atmosphere. At a given
 209 date and location, the dust opacity is set to be the minimum observed over MY
 210 24-31, and further decreased by 50%.
- 211 • A *warm* scenario which corresponds to “dusty atmosphere” conditions, outside of
 212 global dust storms. The dust opacity at a given location and date is set to the max-
 213 imum observed over MY 24-31, excluding the periods of the MY 25 and MY 28
 214 global dust storms, and further increased by 50%.

215 These scenarios are used in the Mars Climate Database (MCD, Millour et al. (2018)),
 216 and frame well the different temperature observations made by several spacecrafts at a
 217 $3\text{-}\sigma$ level (Millour et al., 2018) ($3\text{-}\sigma$ means that 99.7% of the excursions of the value from
 218 the mean are under three standard deviations). Using these scenarios, our simulations
 219 show that the temperature of the air at an altitude of 1 km can vary by several kelvins.
 220 We consider the worst-case scenario, assuming that the *cold* scenario decreases the tem-

221 perature by 10 K compared to the *clim* scenario; and the *warm* scenario increases the
 222 temperature by 10 K (simulations report a maximum of ± 8 K in terms of anomaly, and
 223 we add a 2 K margin). The relative errors made in the interpolation by using these tem-
 224 perature deviations instead of nominal temperatures are presented in Figure 1c. This
 225 sensitivity study shows that the relative $3\text{-}\sigma$ accuracy of this interpolation method is al-
 226 most 1%, and is thus acceptable to exploit MSL pressure data. In summary, we found
 227 that an accurate way to interpolate surface pressure from a point B to a point A at a
 228 local scale consists of using Eq. 1 with the scale height computed using the temperature
 229 at an altitude of 1 km above point B (Eq. 2).

230 **2.2 Large-scale pressure interpolation**

231 At the planetary scale, in addition to the hydrostatic adjustment and local dynamic
 232 effects, we must take into account large-scale dynamic pressure gradients in the inter-
 233 polation (Hourdin et al., 1993, 1995). Hence, interpolating Viking pressure to InSight
 234 cannot be done by using Eq. 1 alone, as it does not consider these gradients.

235 To account for these atmospheric large-scale dynamic components, we use a method
 236 based on the LMD GCM (Hourdin et al., 1993; Forget et al., 1999). Practically, the in-
 237 terpolation of Viking pressure data to obtain the pressure to any location on Mars con-
 238 sists of determining the spatial variation of surface pressure in the GCM, with interpo-
 239 lation from the coarse GCM topography grid (5.625° in longitude, 3.75° in latitude) to
 240 the high-resolution MOLA grid (32 pixels per degree), plus a correction to perfectly match
 241 the seasonal variations at the Viking 1 site.

242 Thus, the interpolation of Viking 1 surface pressure at any location, P_s , is done with
 243 (Forget et al., 2007; Spiga et al., 2007):

$$P_s = \langle P_{\text{Viking}} \rangle \frac{P_{\text{GCM}}}{\langle P_{\text{GCM, Viking}} \rangle} e^{-\frac{z-z_{\text{GCM}}}{H}} \quad (3)$$

244 where P_{GCM} is the pressure predicted by the GCM at the site we want to inter-
 245 polate to, $\langle P_{\text{Viking}} \rangle$ corresponds to the pressure records of Viking averaged over 15
 246 sols to remove any weather variations (thermal tides and transient waves), $\langle P_{\text{GCM, Viking}} \rangle$
 247 is the surface pressure predicted by the GCM at the location of Viking 1 and also smoothed
 248 over 15 sols. $z - z_{\text{GCM}}$ is the difference between the MOLA altitude and the altitude
 249 defined with the interpolation of the GCM topography grid at the location we consider,
 250 and H corresponds to the scale height computed with Eq. 2 using the air temperature
 251 at the site we want to interpolate the Viking measurements. The same procedure as the
 252 one used in section 2.1, using the GCM pressure field binned every 2 hours, again shows
 253 that we must consider the temperature at an altitude of 1 km above the surface. In this
 254 expression (Eq. 3), $\langle P_{\text{Viking}} \rangle$ is the pressure we want to interpolate, $\frac{P_{\text{GCM}}}{\langle P_{\text{GCM, Viking}} \rangle}$
 255 is the correction of atmospheric dynamics induced by the pressure gradients, and $e^{-\frac{z-z_{\text{GCM}}}{H}}$
 256 is a hydrostatic correction, taking into account the effect of local dynamics.

257 We use in this study the Viking 1 surface pressure data rather than Viking 2 data.
 258 Viking 1 data are indeed more complete after removing the measurements made during
 259 dust storms, less sensitive to baroclinic activity (Ryan & Sharman, 1981; Tillman, 1988;
 260 Tillman et al., 1993), and closer to InSight than Viking 2 (Morris & Jones, 1980; Golombek
 261 et al., 2020), thus limiting the sensitivity to errors in the correction of the dynamics of
 262 the atmosphere.

263 The uncertainty of the interpolation depends on two independent uncertainties: one
 264 linked to the Viking 1 pressure measurements and one to the weather-induced uncertainty.
 265 On the one hand, pre-flight tests showed that the precision of the Viking pressure sen-
 266 sors was better than $\pm 0.2\%$ of the readings, plus a term due to a temperature depen-

267 dency of nearly 0.18% (Seiff & Kirk, 1977; Mitchell, 1977). Consequently, the precision
 268 of the pressure measurements was ± 3.4 Pa for Viking 1. Such errors in the precision can
 269 be mitigated, however, as we are using a pressure signal averaged over 15 sols. Assum-
 270 ing that this precision error on a single measurement can be modeled by white noise with
 271 a $3\text{-}\sigma$ of 3.4 Pa, we can reduce the uncertainty on the diurnal average pressure value by
 272 a factor \sqrt{N} where N is the number of measurements used for the diurnal or 15 sols av-
 273 erage. Typically, 200 measurements per sol are used to compute the diurnal average (Barnes,
 274 1980). Therefore, by using a 15 sols averaged surface pressure in Eq. 3, the relative sen-
 275 sitivity to the uncertainty of Viking measurements is limited to 0.06 Pa, and is thus com-
 276 pletely negligible in the following.

277 On the other hand, Viking measurements are also impacted by systematic errors
 278 due to the instrumental drift, the 8-bit telemetry resolution, and the uncertainty on the
 279 zero level of the pressure sensor’s output voltage. Based on the apparent stability of the
 280 sensor because of the great repeatability of the pressure data from one year to another
 281 outside dust storm periods (Hess et al., 1980; Tillman et al., 1993), the instrumental drift
 282 had been estimated to be only -0.1 ± 1 Pa per Earth year and will be neglected in the
 283 following. One could assume that long-term atmospheric changes can be compensated
 284 by the sensor drift, canceling thus the interannual variability in the Viking measurements.
 285 This assumption has been ruled out as it appears very unlikely, based on the accurate
 286 agreement with the mean surface pressure and harmonic analysis (Hess et al., 1980; Till-
 287 man et al., 1993). The error due to the 8-bit telemetry resolution (Seiff, 1976; Tillman
 288 et al., 1993) yields an uncertainty of at most 8.8 Pa in the absolute pressure level for one
 289 single measurement, even if the sensor has a theoretical resolution of nearly 1 Pa (Hess
 290 et al., 1976; Seiff & Kirk, 1977). Assuming that this uncertainty on a single measure-
 291 ment can be modeled by white noise with a $3\text{-}\sigma$ of 8.8 Pa, and using a 15 sols averaged
 292 surface pressure, this uncertainty is reduced to 0.16 Pa and will also be neglected in the
 293 following. The last systematic error related to Viking data is due to the uncertainty on
 294 the zero level of the pressure sensor’s output voltage. This was determined by readings
 295 taken just before atmospheric entry. The resolution uncertainty in these zero readings
 296 causes an uncertainty of up to 8.8 Pa in the absolute pressure level (Seiff & Kirk, 1977;
 297 Kahanpää et al., 2021). Hess et al. (1980) proposed adding 4.4 Pa to each measurement
 298 as it should be the best estimate of the true pressure measurements, reducing the ab-
 299 solute error by half. However, it remains unclear if this adjustment has been implemented
 300 in the Planetary Data System (PDS) where data are available. We will thus consider in
 301 the rest of the study that the absolute error on Viking 1 pressure measurement is $\Delta P_{\text{Viking}} =$
 302 8.8 Pa at a $3\text{-}\sigma$.

303 The second uncertainty in the interpolation is the influence of weather conditions,
 304 which impacts T and thus H in Eq. 3 as well as the pressure predicted in the GCM. To
 305 study the impact of these conditions on the GCM output, we compute the interpolation
 306 of Viking 1 pressure to the InSight landing site by using the three dust scenarios described
 307 above, as they bracket well the possible states of the atmosphere (Millour et al., 2018).
 308 We then compute the weather-induced uncertainty, defined as the relative difference be-
 309 tween the pressure at InSight’s location derived with the extreme dust scenarios (*cold*
 310 and *warm*) and the *clim* dust scenario (Figure 1d). Figure 1d underlines that this weather-
 311 induced uncertainty is generally limited to 1% of the absolute pressure at $3\text{-}\sigma$. We set
 312 this uncertainty as 1% of the mean annual pressure of 700 Pa at InSight’s landing site
 313 (Figure 2), i.e., by $\Delta P_{\text{weather}} = 7$ Pa at $3\text{-}\sigma$. It should be noted that we use dust sce-
 314 narios derived from Mars Climate Sounder (MCS, McCleese et al. (2007)) observations
 315 from MY 29 to MY 35 (Montabone et al., 2015, 2020) for our comparisons. The weather-
 316 induced uncertainty is therefore much lower as these accurate observational scenarios help
 317 to compute T , and thus H , in Eq. 3 precisely.

318 Combining the independent uncertainty of Viking measurements ΔP_{Viking} and the
 319 weather-induced uncertainty $\Delta P_{\text{weather}}$ yields an uncertainty of the interpolation of nearly

320 $\sqrt{8.8^7 + 7^2} \approx 11.2$ Pa at $3\text{-}\sigma$. Such a threshold is at the limit of the lowest predic-
 321 tions of atmospheric mass variations possibly indicated by cap studies (Thomas et al.,
 322 2016), but well below the first estimates made at the beginning of the 2000s (Malin et
 323 al., 2001; Blackburn et al., 2010).

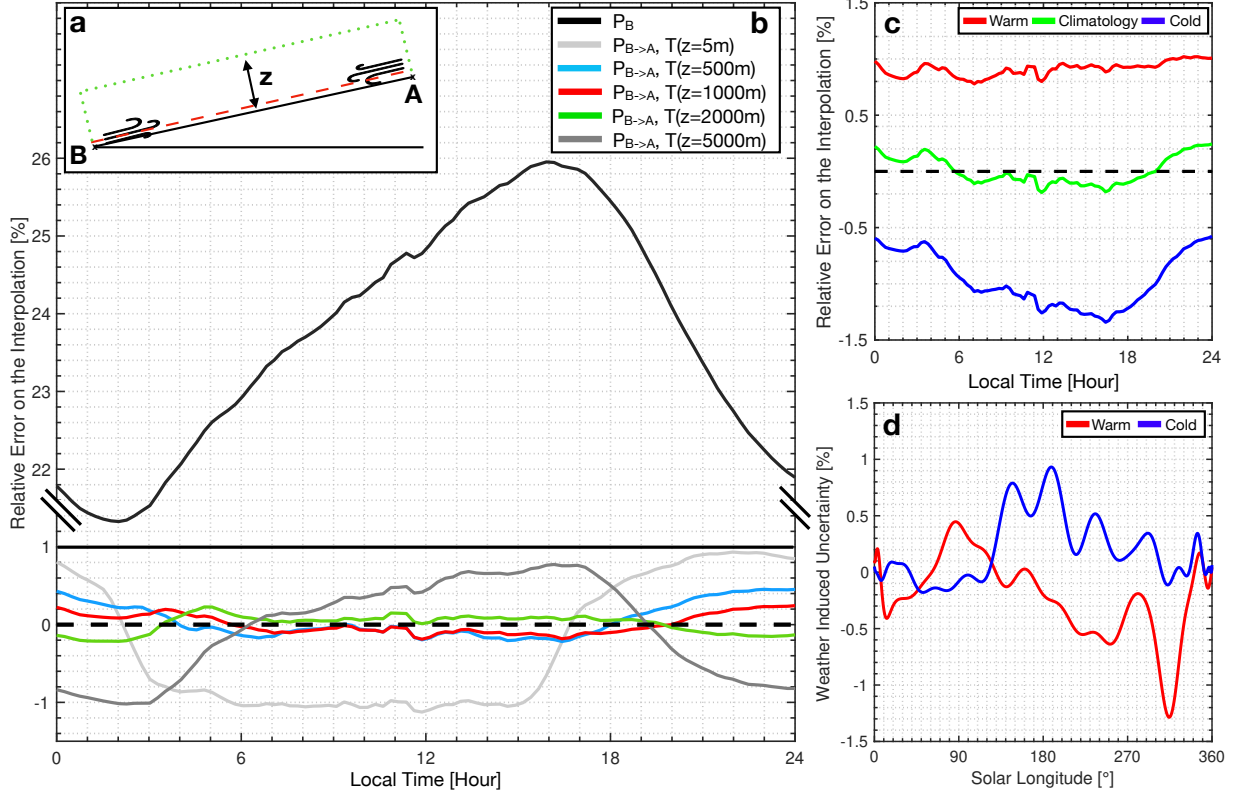


Figure 1. a) Schematics of the problem of interpolation with slope winds between the bottom of Gale Crater (point B) and the rim of the crater (point A). Colored dots illustrate the different paths that can be taken to integrate the hydrostatic equation. b) Relative error of the interpolated pressure from point B to point A and the exact pressure at A. The black curve is the relative error when point B is not interpolated to point A, while colored curves are for the relative errors when using different altitudes for the temperature. The air temperatures T used in the interpolations are computed at an altitude z above point B. c) Relative error on the local interpolation when using the temperature at 1 km above the surface at point A when considering several kinds of weather scenarios. Results are given for the mesoscale simulation that ran for $L_s = 180^\circ$, but similar results (i.e., same magnitudes) are obtained at other L_s . d) Weather-induced uncertainty of the Viking surface pressure interpolated to InSight landing site computed with extreme dust scenarios when compared to *clim* dust scenario (red and blue curves).

324 3 Recalibration of InSight Pressure Data

325 The InSight pressure sensor is located on the lander deck at a height of approx-
 326 imately 1.2 m, with a sampling rate of up to 20 Hz and a noise level lower than 10 mPa,
 327 which theoretically represents an unprecedented quality compared to the different pres-
 328 sure sensors that have operated on the surface of Mars (Banfield et al., 2019, 2020; Spiga

329 et al., 2018). These data are calibrated by using output voltage and pressure sensor tem-
 330 perature channels. We use in this study the 20 Hz data and average them with a 50s win-
 331 dows to remove any effects of high-frequency pressure events (e.g., Chatain et al. (2021);
 332 Spiga et al. (2021)). We then compute the diurnal average of these signals. To do so, we
 333 interpolate the data from previous and following sols to complete the diurnal cycle when
 334 there are small gaps (typically of a few hours) in the data. We then interpolate the mea-
 335 surements onto a regular temporal grid containing 100 points per sol. From these inter-
 336 polated points, we compute the diurnal average. The diurnally averaged surface pres-
 337 sure obtained for the entire dataset (~ 1.25 MY) is presented in Figure 2a.

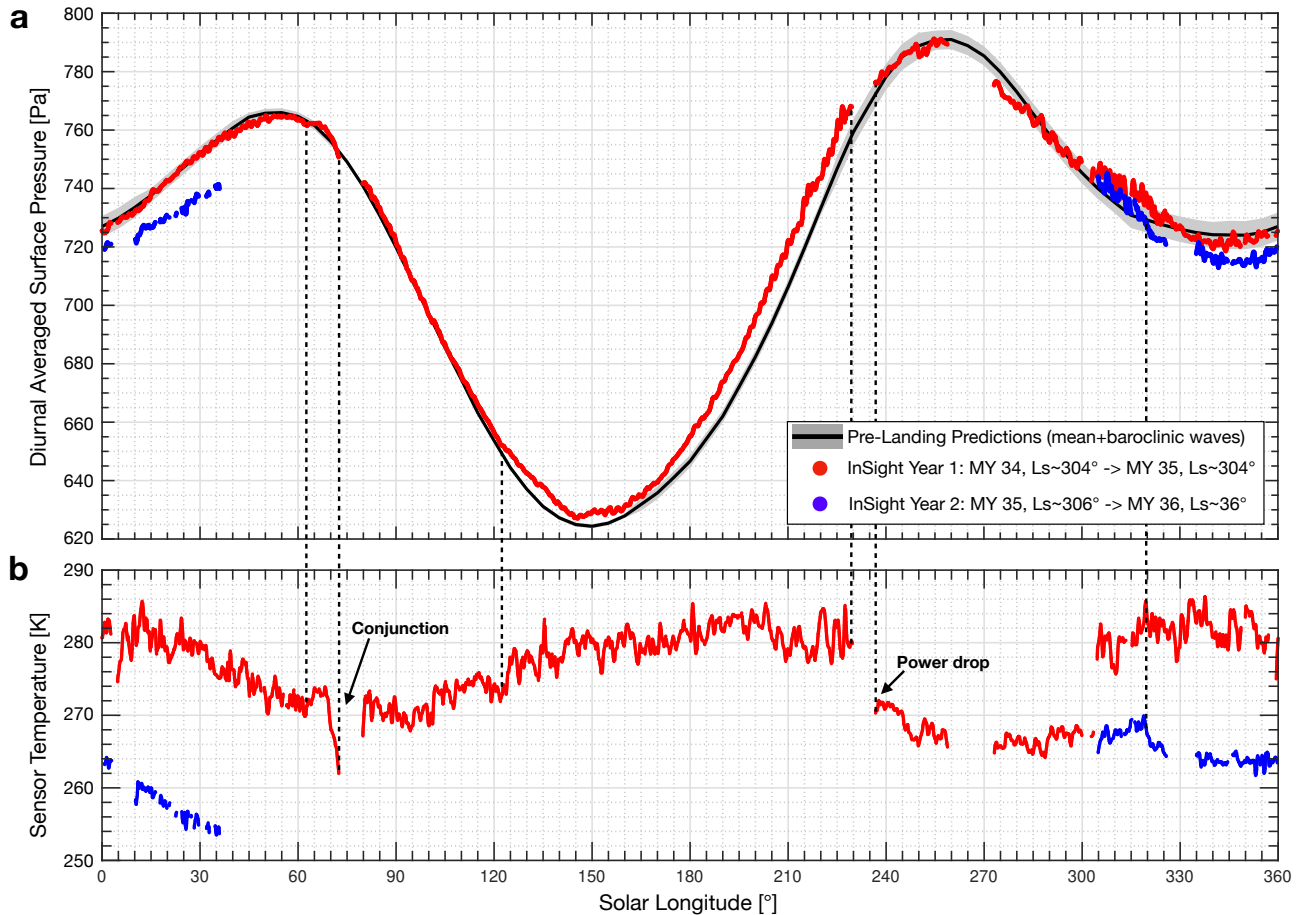


Figure 2. a) Diurnal averaged surface pressure computed from the 20 Hz data acquired during the two years of the mission (red and blue), with pre-landing surface pressure predictions (black curve) and baroclinic waves amplitudes (grey filled area) from Spiga et al. (2018). b) Diurnal averaged temperature of the pressure sensor. Red dots are for the first year of the mission, while blue dots represent the measurements taken during the second year of the mission. Dashed black lines highlight the significant correlations between the pressure sensor temperature and the pressure measurements.

338 3.1 Sensor temperature sensitivity of the InSight pressure data

339 A direct comparison between the pressure measurements made one year apart dur-
 340 ing the first and second martian years of the InSight mission shows a large difference (Fig-

341 ure 2). This cannot be explained by the instrumental drift reported in Banfield et al. (2019);
 342 Spiga et al. (2018) or by any likely major meteorological event as no significant long-lived
 343 global events have been observed. This difference is also not observed by MSL pressure
 344 measurements (Figure S1), thus questioning the reliability of the InSight pressure mea-
 345 surements. Furthermore, the divergence between the measurements made two years apart
 346 seemed to increase toward the end of the mission, when the power allocated to the pres-
 347 sure sensor was very low because of the accumulation of dust on the solar panels, lead-
 348 ing to a decrease of the pressure sensor temperature. In the following, sensor temper-
 349 ature will refer to the temperature of the pressure sensor and does not refer to other tem-
 350 peratures (e.g. TWINS air temperature (Banfield et al., 2019) or other sensor temper-
 351 atures measured by InSight).

352 A close comparison of the pressure measurements and sensor temperature (Figure
 353 2b) reveals that the pressure measurements are very likely to be affected by some drops
 354 or rises in the sensor temperature. An illustration of this correlation is at $L_s \sim 72^\circ$, just
 355 before conjunction. Sensors were powered off, after the warm Electronics Box had cooled
 356 off, and a nonphysical drop occurred in the pressure measurements. This correlation ques-
 357 tions the reliability of the calibration of the absolute pressure data to the sensor tem-
 358 perature. The pre-flight calibration of the pressure sensor with temperature may not be
 359 as accurate as expected, possibly because of the existence of temperature gradients within
 360 the instrument under real martian conditions. Such an effect had already been identi-
 361 fied as responsible for pressure measurement errors on Phoenix (Taylor et al., 2010). It
 362 is important to note that most of the scientific results obtained from the pressure data
 363 are not impacted by this calibration problem. These works (see for instance Banerdt et
 364 al. (2020); Spiga et al. (2021); Chatain et al. (2021)) use relative pressure variations and
 365 not absolute measurements, and at high frequencies. At these frequencies, i.e., for timescales
 366 of the order of a sol, or less, the fluctuations of the sensor temperature are negligible.
 367 The calibration problem detected is thus nullified when using relative variations of mea-
 368 sured pressures, and therefore does not bias the scientific results obtained. We propose
 369 in section 3.3 to correct this thermal effect using MSL pressure data.

370 **3.2 Mars Science Laboratory pressure data**

371 In the absence of major meteorological events, we can expect limited interannual
 372 variations between the pressure measured during the first and the second year of the In-
 373 Sight mission (see legend of Figure 2 for definitions). de la Torre Juarez et al. (2019) re-
 374 ported a strong interannual variability of the pressure data at the end of MY 34 and the
 375 beginning of MY 35 compared to other years using MSL pressure data (Figure S1). Such
 376 a difference might be linked to the global dust storm of MY 34 that possibly had an im-
 377 pact on the extent of the NSPC.

378 To take into account a possible interannual variability between InSight’s first and
 379 second years of the mission, we use MSL Rover Environmental Monitoring Station (REMS)
 380 pressure data available in the PDS. The calibrated data extracted from the PDS extend
 381 from MY 31, at a solar longitude (L_s , the Mars-Sun angle, measured from the North-
 382 ern Hemisphere spring equinox where $L_s=0^\circ$) $L_s \sim 150^\circ$, to MY 36, $L_s \sim 21^\circ$. The REMS
 383 pressure sensor acquires data during the first five minutes of each Local Mean Solar Time
 384 (LMST) with additional hour-long acquisitions that cover a full diurnal cycle about ev-
 385 ery 6 sols (Gómez-Elvira et al., 2014). To take into account the vertical displacement
 386 of the rover on pressure measurements that could account for more than 15 Pa in the
 387 pressure records (Ordóñez-Etxeberria et al., 2019), we interpolate the pressure data from
 388 the position of the rover, determined with the Ancillary Data Record (ADR) files, to the
 389 MSL landing site using the method described in section 2.1, Eq. 1. The air temperatures
 390 at an altitude of 1 km above the surface are computed with the MCD, using dust sce-
 391 narios from Montabone et al. (2015, 2020) as inputs for the simulations. The results of
 392 this interpolation are presented in Figure S1. The correction of these altitude differences

393 can reach 20 Pa (more than Ordonez-Etxeberria et al. (2019) because we use a larger
 394 dataset). We obtain a dataset with little interannual variability, except during the end
 395 of MY 34 and the beginning of MY 35, as noted by de la Torre Juarez et al. (2019). This
 396 good repeatability in our corrected MSL pressure dataset further validates our interpo-
 397 lation method presented in section 2.1 to correct altitude differences.

398 3.3 Recalibration of the pressure measurements

399 We define $E(T(t))$ (in Pa) as the sensitivity of the pressure measurements with re-
 400 gards to the sensor temperature T . The corrected measured pressure $P_{\text{InSight,Corrected}}$
 401 at a time t can be written as:

$$P_{\text{InSight,Corrected}}(t) = P_{\text{InSight,Measured}}(t) + E(T(t)) \quad (4)$$

402 We average the pressure measured by MSL and InSight over 15 sols to eliminate
 403 the contribution of any dynamical component like thermal tides and baroclinic activity.
 404 These averaged pressure values are denoted $\langle P \rangle$ in the following. As InSight and
 405 MSL are relatively close (~ 600 km), we assume that the correction of the large-scale
 406 atmospheric dynamics between the two sites can be neglected. Our simulations show in-
 407 deed that this correction is limited to 1 Pa at $3\text{-}\sigma$ and is thus negligible.

408 During InSight year 1 (Y_1 : MY 34, $L_s \sim 304^\circ$ to MY 35, $L_s \sim 304^\circ$) and year 2
 409 (Y_2 : MY 35, $L_s \sim 306^\circ$ to MY 36, $L_s \sim 36^\circ$) of the mission, we have:

$$\begin{cases} \langle P_{\text{InSight,Corrected}}(t_{Y_1}) \rangle = \langle P_{\text{MSL}}(t_{Y_1}) \rangle e^{-\frac{\Delta z}{H(t_{Y_1})}} \\ \langle P_{\text{InSight,Corrected}}(t_{Y_2}) \rangle = \langle P_{\text{MSL}}(t_{Y_2}) \rangle e^{-\frac{\Delta z}{H(t_{Y_2})}} \end{cases} \quad (5)$$

410 with Δz the difference of altitude between the InSight and MSL landing site, and H the
 411 scale height computed with the air temperature at an altitude of 1 km above the sur-
 412 face of Gale crater. GCM computations show that with MY 34, 35 and *clim* dust sce-
 413 narios, we have to first order $e^{-\frac{\Delta z}{H(t_{Y_1})}} \sim e^{-\frac{\Delta z}{H(t_{Y_2})}}$. Thus Eq. 5 leads to:

$$\frac{\langle P_{\text{InSight,Corrected}}(t_{Y_1}) \rangle}{\langle P_{\text{InSight,Corrected}}(t_{Y_2}) \rangle} = \frac{\langle P_{\text{MSL}}(t_{Y_1}) \rangle}{\langle P_{\text{MSL}}(t_{Y_2}) \rangle} = \beta \quad (6)$$

414 where β is by definition the interannual variability between the two years of mea-
 415 surements. Hence, as we only use a ratio of pressures, the absolute pressure values mea-
 416 sured by MSL do not impact the absolute values of InSight pressure measurements af-
 417 ter being corrected, and thus do not introduce a bias in our comparison. The problem
 418 described by Eq. 6 can be transformed into the following optimization problem:

Find E that minimizes :

$$\| \langle P_{\text{InSight,Corrected}}(t_{Y_1}) \rangle - \beta \langle P_{\text{InSight,Corrected}}(t_{Y_2}) \rangle \| \quad (7)$$

419 where $\| \cdot \|$ refers to the Euclidean norm. Introducing Eq. 4 into 6 gives:

$$\begin{aligned} \langle P_{\text{InSight,Measured}}(t_{Y_1}) \rangle - \beta \langle P_{\text{InSight,Measured}}(t_{Y_2}) \rangle \\ = \beta \langle E(T(t_{Y_2})) \rangle - \langle E(T(t_{Y_1})) \rangle \end{aligned} \quad (8)$$

420 We further assume that E can be written as a polynomial function of the sensor
421 temperature:

$$E(T(t)) = \sum_{k=0}^n \alpha_k T(t)^k \quad (9)$$

422 Introducing this into Eq. 8 finally leads to:

$$\begin{aligned} \langle P_{\text{InSight,Measured}}(t_{Y_1}) \rangle - \beta \langle P_{\text{InSight,Measured}}(t_{Y_2}) \rangle \\ = \sum_{k=0}^n \alpha_k \langle \beta T(t_{Y_2})^k - T(t_{Y_1})^k \rangle \end{aligned} \quad (10)$$

423 This last equation represents a least-mean-square problem that can be solved nu-
424 merically to determine the coefficients α_k of E for a given degree n . However, the prob-
425 lem must be constrained to have a physical solution. The first term α_0 is indeed poorly
426 constrained as $\beta \sim 1$ (β ranges from 0.992 to 0.998 during the period considered below)
427 and thus $\langle \beta T(t_{Y_2})^0 - T(t_{Y_1})^0 \rangle \sim 0$. A close look at Figure 2 reveals an unex-
428 pected increase of the uncorrected pressure at $L_s \sim 63^\circ$ (suggesting that E should be neg-
429 ative), and then a drop (suggesting that E should be positive), both certainly resulting
430 from a rise of temperature at $T = 270$ K and followed by a decrease of temperature at
431 $T = 275$ K. Such observations are also found at $L_s = 120^\circ$ and 290° , suggesting a change
432 of behavior of the sensor temperature sensitivity, i.e., a change in the sign of $E(T)$ close
433 to $T = 273$ K (with $E(T > 273\text{K}) > 0$ and $E(T < 273\text{K}) < 0$). Hence we simply
434 assume that:

$$E(T = 273 \text{ K}) = 0 \text{ Pa} \quad (11)$$

435 The resolution of the problem is made as follows. For each degree n , we compute
436 the coefficients α_k with a least mean square algorithm based on Eq. 10 and 11 to have
437 E . We then compute $\| \langle P_{\text{InSight,Corrected}}(t_{Y_1}) \rangle - \beta \langle P_{\text{InSight,Corrected}}(t_{Y_2}) \rangle \|$ us-
438 ing Eq. 4. We iterate on the degree n to find which E is solution of the optimization prob-
439 lem described in Eq. 7.

440 To compute the least-mean square inversion, we use the data acquired at the end
441 of the MY 34, at $L_s > 340^\circ$ to remove the effect of local dust storms, and data at $L_s <$
442 21° (the limit of the MSL dataset that we used). We find that increasing the degree of
443 E reduces the norm of $\langle P_{\text{InSight,Corrected}}(t_{Y_1}) \rangle - \beta \langle P_{\text{InSight,Corrected}}(t_{Y_2}) \rangle$. How-
444 ever, polynomial corrections with high degree n induce non-physical behavior of the cor-
445 rections, especially for the edges of the sensor temperature range (e.g., $T \sim 250$ K). We
446 complete thus our test by investigating which degree minimise the absolute difference
447 $|\langle P_{\text{InSight,Corrected}}(t_{Y_1}) \rangle - \beta \langle P_{\text{InSight,Corrected}}(t_{Y_2}) \rangle|$ so that our correction will
448 give realistic solution for the complete range of sensor temperature correction. With these
449 two criteria, we find that $n = 3$ is the solution that reduces the euclidean norm and min-
450 imizes the absolute value of $\langle P_{\text{InSight,Corrected}}(t_{Y_1}) \rangle - \beta \langle P_{\text{InSight,Corrected}}(t_{Y_2}) \rangle$.
451 This fit has also been validated with some goodness of fit criteria ($R^2 \sim 0.93$, reduced
452 $\chi^2 \sim 0.94$). The final correction E (in Pa) can be at least written as a function of the
453 sensor temperature T (in K):

$$E(T) \approx 5.5273 \times 10^{-4} T^3 - 0.4284 T^2 + 109.6849 T - 9.2602 \times 10^3 \quad (12)$$

454 This correction is presented in Figure 3. This correction add ± 5 Pa to the pres-
455 sure measurements in the range of the sensor temperatures measured most often dur-

456 ing the mission (Figure 2). The correction is significant at very low temperatures (e.g.,
 457 $T < 260$ K), as expected when looking at the drop of the surface pressure measured
 458 at the end of the mission. Finally, we logically find that $E(T < 273 \text{ K}) < 0$ and $E(T <$
 459 $273 \text{ K}) > 0$.

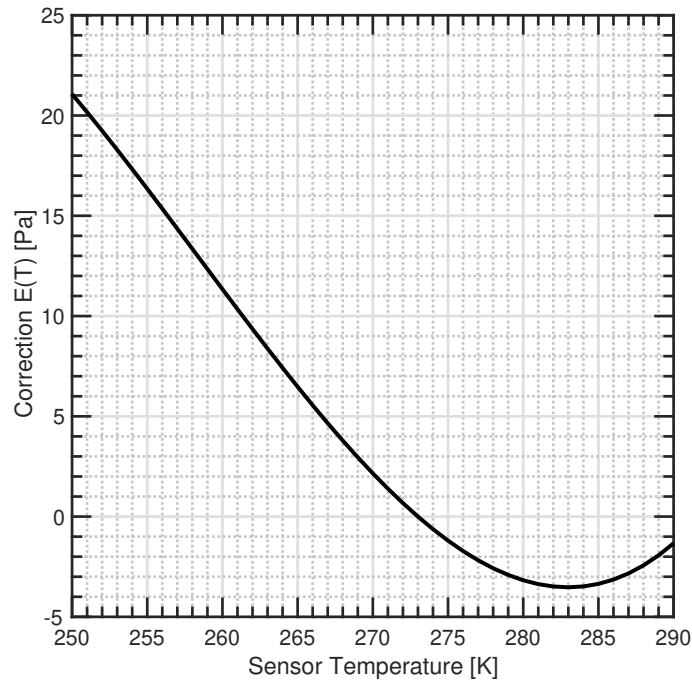


Figure 3. Correction of the thermal sensitivity E applied on the pressure measurements vs sensor temperature T .

460 Applying this correction to the complete measured pressure data with Eq. 4 leads
 461 to the result presented in Figure 4. As expected, this correction strongly modifies the
 462 pressure measured by InSight in terms of amplitude and shape. The Northern winter sur-
 463 face pressure during InSight Year 1 is lower than during InSight Year 2, but tends to equal-
 464 ize during spring. These results are thus consistent with the analysis of contemporary
 465 MSL data from de la Torre Juarez et al. (2019) who also observed a pressure deficit at
 466 the end of MY 34 and the beginning of MY 35 when studying the interannual variabil-
 467 ity of MSL pressure data.

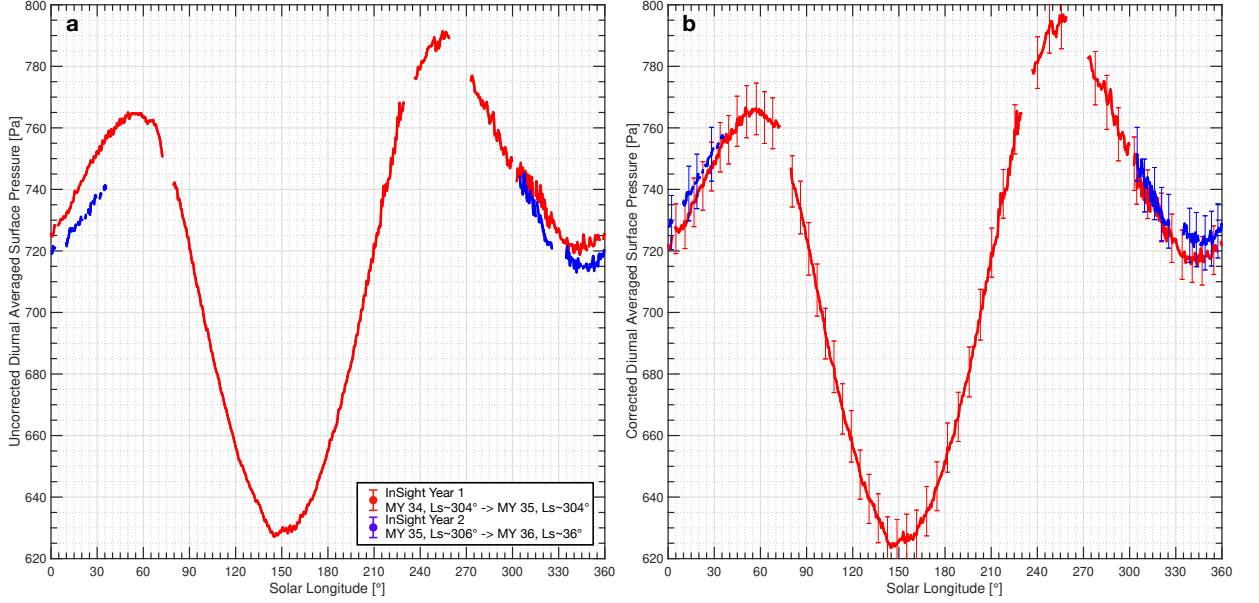


Figure 4. a) Diurnal averaged surface pressure computed from the raw pressure data. b) Diurnal averaged surface pressure after applying the thermal correction. Error bars represent the uncertainty on the measurements after the correction at $3\text{-}\sigma$. The details of the uncertainty computations are described in the text. Red dots are for the first year or the mission, while blue dots are for the second year.

468

3.4 Uncertainty of the corrected data

469

470

471

472

473

474

475

476

477

478

479

480

481

482

483

484

The accuracy of InSight pressure measurements is crucial for the determination of possible secular pressure changes and will be useful to the community for future scientific work. We thus need to quantify the uncertainty of the InSight corrected pressure proposed in section 3.3. Three kinds of uncertainty can be highlighted here according to Eq. 4. The first one is the uncertainty of the pressure sensor on the measurement, which is $\sigma_{P_{sensor}} = 1.5$ Pa R.M.S (Banfield et al., 2019). The second one is caused by the uncertainty of the correction. This correction deals with the uncertainties at $1\text{-}\sigma$ of the pressure measured by InSight $\sigma_{P_{sensor}}$ and the sensor temperature uncertainty σ_T set here at 1 K. However, the uncertainty of β , and thus the impact of MSL uncertainty on our correction, is negligible. ($\frac{\sigma_\beta}{\beta} \ll 1$, Appendix A). Hence, as we use a ratio of MSL pressure measurements to derive the interannual variability β of the InSight pressure data, the absolute MSL pressure accuracy does not impact the accuracy of our correction for the InSight pressure measurements. Finally, an uncertainty is associated with the choice of the temperature nullifying the correction term (Eq. 11); this last one having been made arbitrarily after analysis of the correlations between the measured pressure and the sensor temperature.

485

486

487

488

489

490

491

492

493

To derive the uncertainty in E at a sensor temperature T ($\Delta E(T)$), we perform a Monte Carlo error analysis as described in Press et al. (1993) or Forget et al. (2007). We generate an ensemble of 10^4 inputs (P_{InSight}, T), affected by the various uncertainties described above. All the input parameters are computed using their nominal values plus random values computed from a normal distribution with a standard deviation associated with $\sigma_{P_{sensor}}, \sigma_T$. The condition provided in Eq. 11 is also perturbed using a normal distribution with a standard deviation of σ_T . We then apply our algorithm to retrieve the thermal correction E at a given sensor temperature T with these inputs. We finally compute the standard deviation of the E provided. We find that the distribution

494 of the E retrieved follows a normal distribution as illustrated in Figure 5a. The stan-
 495 dard deviation of the fitted normal distribution gives the uncertainty of $E(T)$ at $1-\sigma$.
 496 We apply this Monte Carlo analysis for temperatures ranging from 250 K to 290 K to
 497 retrieve $\sigma_{E(T)}$, i.e., the uncertainty at $1-\sigma$ level. The results from this computation are
 498 presented in Figure 5b. The variations of this curve follow the variations of the gradi-
 499 ent of $E(T)$. We then do a least mean square polynomial fit to have an empirical law
 500 to simply deduce $\sigma_{E(T)}(T)$:

$$\sigma_{E(T)}(T) = 5.1453 \times 10^{-5} T^3 - 0.0418 T^2 + 11.2738 \times T - 1.0109 \times 10^3 \quad (13)$$

501 We finally retrieve the $3-\sigma$ uncertainty of one pressure measurement by combin-
 502 ing these two uncertainties, plus a term due to the dependence between the measurement
 503 and the thermal correction, as the raw measurements and temperature are correlated due
 504 to the initial calibration procedure:

$$\Delta P_{InSight}(T) = 3 \times \sqrt{(\sigma_{P_{sensor}})^2 + (\sigma_{E(T)}(T))^2 + 2\sigma_{P_{sensor}}\sigma_{E(T)}(T)\rho_{P_{sensor},T}} \quad (14)$$

505 where $\rho_{P_{sensor},T}$ is the correlation coefficient between the raw pressure measurement P_{sensor}
 506 and the sensor temperature (T), assumed to be 1 as the pressure sensor is calibrated us-
 507 ing the sensor temperature (Banfield et al., 2019). Uncertainties on the corrected pres-
 508 sure range from 7.5 Pa to 8.9 Pa at a $3-\sigma$ level. Such values are close to the magnitude
 509 of the atmospheric mass variations expected based on Thomas et al. (2016) (± 9 Pa dif-
 510 ference between Viking 1 and InSight surface pressures), but are much smaller than the
 511 expected changes that are computed from Blackburn et al. (2010); Malin et al. (2001) ($\sim +25$
 512 Pa difference between Viking 1 and InSight surface pressure). We therefore consider that
 513 the InSight corrected pressure data are accurate enough to detect such secular pressure
 514 changes.

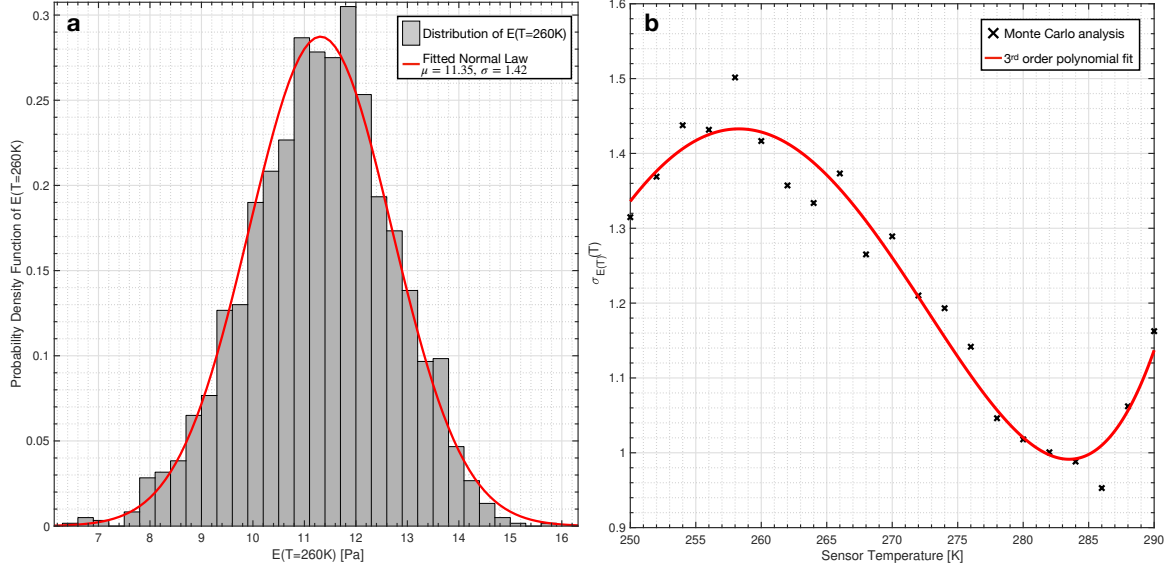


Figure 5. a) Monte Carlo analysis to retrieve $\sigma_{E(T=260K)}$. The histogram of the samples is presented in gray and is normalized to obtain a probability density function. The fitted normal law is illustrated in red and has as parameters the mean μ and the standard deviation of the distribution σ . b) Empirical law for $\sigma_{E(T)}(T)$ obtained from Monte Carlo analysis (black cross) and 3rd order polynomial fit of this law (red line)

515

3.5 Comparison with MSL pressure data and validation

516

517

518

519

520

521

522

523

524

525

To test the reliability of our correction, we propose here to compare the corrected InSight pressure to the MSL pressure measurements interpolated to the InSight landing site. This comparison is relevant as the use of the MSL data to correct the InSight data relied on the year-to-year ratio (Eq. 6), and thus does not influence seasonal variation given by InSight pressure data after the correction. To do so, we use the methodology described in 2.2 by using the ratio $\frac{P_{MSL}}{P_{GCM,MSL}}$ into Eq. 3, with MY 34, 35 and *clim* dust scenario for the beginning of MY 36. The comparison between interpolated MSL pressure and InSight measurements is presented in Figure 6. There is an overall good agreement between the InSight corrected measurements and the MSL pressure measurements. This consistency strengthens the credibility of our correction.

526

527

528

529

530

531

532

We note a deficit δ of pressure between MSL pressure interpolated at the InSight landing site, and InSight corrected pressure between $L_s \sim 220^\circ$ and $L_s < \sim 360^\circ$ (Figure 6). This deficit represents $\sim 1\%$ of InSight surface pressure and could reach 8 to 10 Pa. Three causes could explain this deficit: 1) a dynamical effect that is not included in our interpolation process 2) a meteorological effect that changes the thermal state of the atmosphere, and thus the scale height used during the interpolation 3) a problem with our correction.

533

534

535

536

537

538

539

540

As InSight and MSL are close to each other (~ 600 km), the impact of atmospheric dynamics on the interpolation is limited. As underlined by Figure 6b, the deficit δ remains when correcting the large-scale pressure gradients. Therefore, these large-scale atmospheric dynamics do not explain the pressure deficit δ . Another possible explanation might be the small-scale/regional topography of Gale crater that is not included by our GCM. The two closest points are at a longitude of 135° E and 140.6° E, with an altitude of -2069 and -1879 m respectively. The interpolation using the four closest points of the GCM to the MSL landing site gives an altitude of -1544m, far from the actual landing

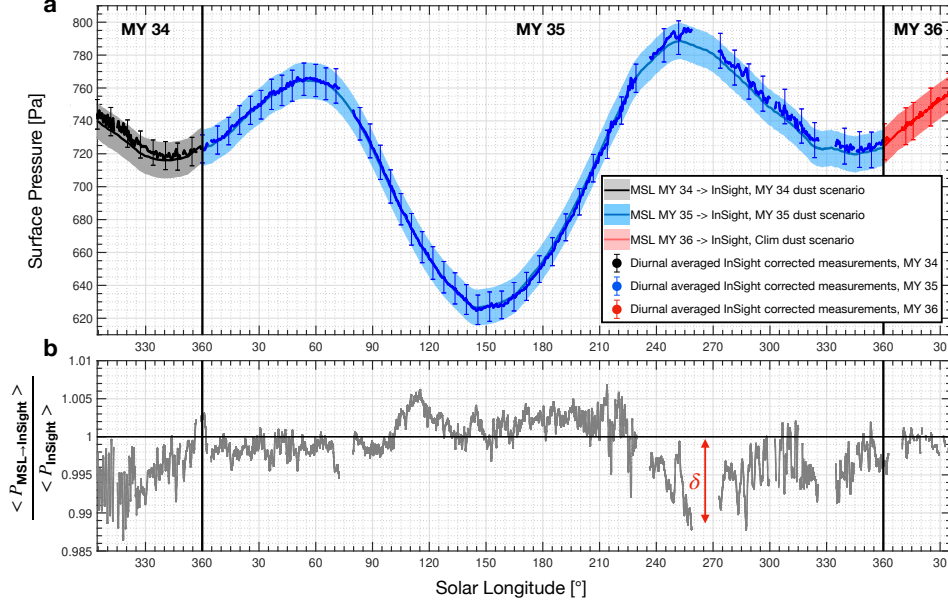


Figure 6. a) Comparison between the surface pressure measured by InSight and that measured by MSL but interpolated to the InSight landing site, for MY 34, 35, and 36. The filled box around the plain line depicts the $3\text{-}\sigma$ uncertainty of the interpolation due to weather-induced uncertainty and MSL absolute errors, following the methodology presented in section 2.2. Pressure interpolated is averaged over a period of 15 sols to remove atmospheric tides and baroclinic activity. InSight measurements are diurnally averaged thus still indicate baroclinic activity with periods of several sols. The error bars correspond to the $3\text{-}\sigma$ on InSight corrected pressure measurements as described in section 3.4. b) Evolution of the ratio of MSL REMS pressure measurements interpolated to the InSight landing site, and InSight pressure measurements. Dots correspond to the ratio using the interpolation method described in section 2.2.

541 site altitude of -4501 m. Furthermore, complex crater circulations (Pla-Garcia et al., 2016;
 542 Rafkin et al., 2016) might impact the pressure measured by MSL. To investigate the po-
 543 tential impact of this particular topography (and thus the local circulations, aerosol dis-
 544 tributions, small-scale physical phenomena, etc. (Spiga & Forget, 2009)) on the surface
 545 pressure deficit, we used the mesoscale LMD model simulations described in section 2.1.
 546 We ran the model for 24 hours after initial spin-up time of 24 hours, at $L_s = 270^\circ$. The
 547 mesoscale model, resolving amore accurate topography, helps to reduce the pressure deficit
 548 between MSL interpolated to InSight and InSight measurements by 2-3 Pa. However,
 549 it still not fully explain the difference observed. Hence, the deficit δ does not seem to
 550 be due entirely to a is not due to local dynamic effects, or to the too coarse resolution
 551 of the GCM which does not capture the topography of Gale crater.

552 We then studied this deficit δ by investigating the possible influence of the scale
 553 height H , using the interpolation described in 2.1. Results are presented in Figure 7a.
 554 We observe again the pressure deficit between InSight and MSL after $L_s = 180^\circ$. To study
 555 the influence of the scale height, we compute the temperature T_* such that: $\frac{\langle P_{\text{MSL} \rightarrow \text{InSight}} \rangle}{\langle P_{\text{InSight}} \rangle} \approx 1$.
 556 Using Eq. 1 and 2, T_* writes:

$$T_* = -\frac{\Delta z}{\frac{R}{\mu g} \ln \frac{P_{\text{MSL,measured}}}{P_{\text{InSight,measured}}}} \quad (15)$$

557 where Δz correspond to the difference of altitude between the InSight landing site and
 558 MSL altitude (in meters), and $P_{\text{MSL,measured}}$ is the raw MSL REMS pressure measure-
 559 ments. To detect any anomaly in the temperature, we compare this temperature T_* to
 560 the temperature at an altitude of 1 km above the surface predicted by the GCM (Fig-
 561 ure 7b). This comparison underlines warming by 10-15 Kelvin of the temperature at this
 562 altitude, at $200^\circ < L_s < 360^\circ$.

563 This difference between T_* and the temperature given by the GCM might be ex-
 564 plained by an unexpected accumulation of aerosols within Gale Crater, such as dust, com-
 565 pared to what is assumed in the GCM. The presence of aerosols would indeed warm up
 566 the air as they absorb solar radiation. Moreover, GCM simulations using our *warm* sce-
 567 nario indicate a warming of nearly 5-8 K of this atmospheric layer, which is the order
 568 of magnitude of the anomaly observed here. Hence, by studying the evolution of the tem-
 569 perature anomaly presented in Figure 7b, we could assume that at $L_s > 180^\circ$, there are
 570 local effects that increase the quantity of dust or other aerosols within the crater, induc-
 571 ing a warming of the air temperature. By comparing the measured and interpolated pres-
 572 sures at different local times around $L_s = 275^\circ$ (Figure 7c), we find that this pressure anomaly
 573 is much more significant during the daytime periods than at night. We can assume that
 574 the air within the crater is heated during the day due to the presence of this dust in sus-
 575 pension. This hypothesis is consistent with the REMS temperature observations at the
 576 surface and at 2 m from the ground at this time of year, which are respectively lower and
 577 higher than predicted by mesoscale models (Pla-Garcia et al., 2016).

578 Assuming that Gale crater is full of dust at this time of the year is plausible as sev-
 579 eral observations have shown the large presence of dust within the crater at this time
 580 of the martian year. Measurements of the line-of-sight across-crater extinction with MSL
 581 cameras report an increase of dust loading at lower elevations during the dusty season,
 582 i.e., $180^\circ < L_s < 360^\circ$. The analysis of UV sensors data onboard MSL also confirms this
 583 observation, with net dust lifting from the crater floor during the dusty season, and net
 584 deposition during the rest of the year (Vicente-Retortillo et al., 2018). Such observations
 585 confirmed models of dust diffusion rate within Gale crater (Moore et al., 2019) that re-
 586 port net dust lifting from $L_s \approx 220\text{-}240^\circ$, and net dust deposition in the crater before this
 587 date, explaining the variation of the thermal inertia of the ground (Rangarajan & Ghosh,
 588 2020). This behavior of settling and suspension of dust within Gale might be explained
 589 by the dynamics of the planetary boundary layer within the crater. Fonseca et al. (2018)
 590 points out that at $L_s > 180^\circ$, the planetary boundary layer (PBL) height is higher than
 591 the crater rim for a few hours during the afternoon, inducing a mixing between the air
 592 outside and inside the crater. In addition, dust might be injected within the crater be-
 593 cause of dust devils and wind-driven dust lifting. As reported by Steakley and Murphy
 594 (2016); Kahanpää et al. (2016); Ordonez-Etxeberria et al. (2018); Newman et al. (2019),
 595 there are very strong seasonal variations in dust devil activity, with a peak of that dust
 596 devil lifting around southern spring and summer, i.e., when we observed the pressure deficit
 597 δ . Most of the dust devil occurs during the day, with a peak of activity around noon,
 598 close to the period of the sol when the pressure difference between MSL and InSight is
 599 the most important (Figure 7c).

600 We also obtain indications of the presence of aerosols near the surface using the
 601 THEMIS visible camera (Christensen et al., 2004). Figures 7d and e compare two im-
 602 ages of Gale Crater, at the same local hour, in quasi-similar illumination conditions, but
 603 at two different L_s (130° and 229° respectively). Figure 7e clearly shows the presence
 604 of aerosols (black arrow) confined within the crater, as the portion of Mount Sharp re-
 605 mains easily detectable and less obstructed. Another indication of the presence of a sig-
 606 nificant quantity of aerosols in the air is the difficulty of detecting the ground and the
 607 craters at the bottom of Gale crater on the image e compared to d (see red arrows), in
 608 quasi-similar illumination conditions. Water fog is a suspected candidate to explain this
 609 phenomenon, as the image is taken during the early morning, but it seems highly un-

610 realistic as the relative humidity at this time of the year is at its lowest level (Martínez
611 et al., 2016; Martínez et al., 2017). Furthermore, images taken at nearly 17 hr Local True
612 Solar Time (LTST) also report such features (see for instance THEMIS image *V59356002*
613 that were taken at a quite similar location at $L_s = 335^\circ$, at 17.37 hr). However, opac-
614 ity derived from MSL cameras does not show a significant increase of dust loading at this
615 time, compared to what is predicted by the *clim* scenario (see Figure 9 of Ordonez-Etxeberria
616 et al. (2019)).

617 We acknowledge that these observations are consistent with the presence of dust
618 within the crater, but do not show that Gale crater is abnormally dusty at this time of
619 the year. The Northern fall and winter are indeed expected to be dustier than the begin-
620 ning of the martian year (Kahre et al., 2017), as previously observed at the beginning
621 of MSL mission (Guzewich et al., 2017). Further investigations like Moores et al. (2015);
622 Guzewich et al. (2017) using MY 35 data will help to validate or deny our assumption
623 of an abnormally dusty Gale crater at this time of the year. Nevertheless, our hypoth-
624 esis is still credible because of the large presence of dust within the crater at the time
625 of the year, and has the potential to explain the observed deficit. A major mistake in
626 our correction seems at least unlikely because of the very good agreement between the
627 pressure measurements of MSL and InSight during the rest of the year.

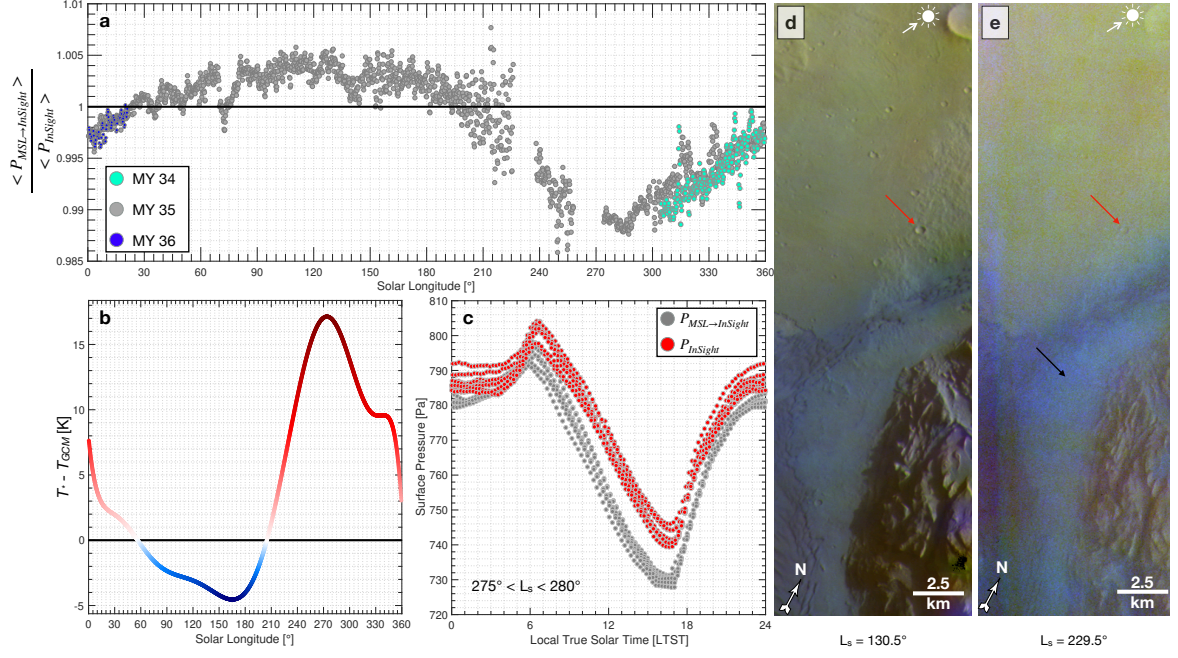


Figure 7. a) Evolution of the ratio of MSL REMS pressure measurements interpolated to the InSight landing site, and InSight pressure measurements. Dots correspond to the ratio using the interpolation method described in section 2.1, i.e., neglecting atmospheric dynamic effects, during MY 34 (green), MY 35 (grey), and MY 36 (blue). b) Anomaly between the temperature of the GCM at an altitude of 1 km above the surface, and the temperature T_* that gives a ratio of 1, as a function of L_s (colored curve) for MY 35. c) Comparison between InSight surface pressure over a complete sol and MSL pressure interpolated at InSight landing site between $L_s = 275^\circ$ and 280° , during MY 35. d) Extract of THEMIS image *V63417011* of Gale Crater (center of the original image: $4.9^\circ\text{S}; 137.0^\circ\text{E}$) taken at $L_s = 130^\circ$, LTST = 7.2hr, with a solar incident angle of 74.5° . e) Extract of THEMIS image *V65575024* at the same location, taken at $L_s = 229^\circ$, LTST = 7.2hr, with a solar incident angle of 71.3° . The black arrow on e) points to the suspected aerosols, whereas the red arrows on d) and e) point to the same crater for a comparison of the perceptibility of the ground. White arrows point to the position of the Sun in the sky.

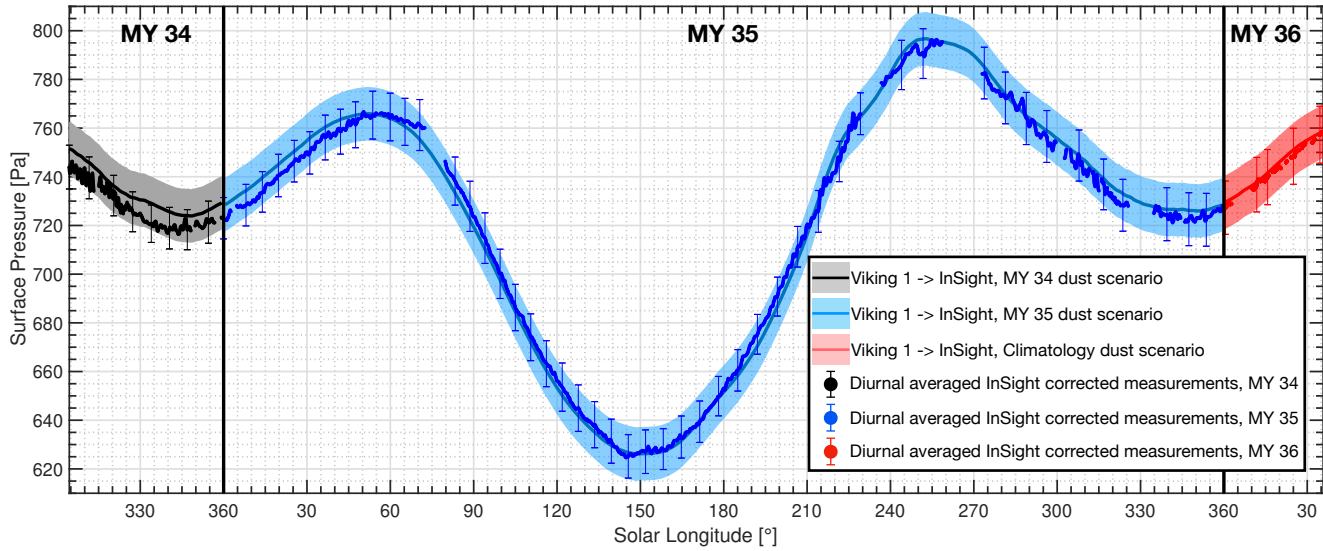
628 **4 Results: Comparison with Viking Lander 1 Pressure Data**

Figure 8. Comparison between the surface pressure by Viking 1 interpolated at the InSight landing site for MY 34, 35, and 36. The filled box around the plain line depicts the $3\text{-}\sigma$ uncertainty of the interpolation detailed in section 2.2. Pressure interpolated is averaged on a period of 15° to remove atmospheric tides and baroclinic activity. InSight measurements are diurnal averaged and still keep baroclinic activity. The error bars correspond to the $3\text{-}\sigma$ on InSight corrected pressure measurements as described in section 3.4.

629 The comparison between the Viking 1 surface pressure measurements interpolated
 630 at the InSight landing site and the InSight temperature-corrected measurements for MY
 631 34, 35, and 36 is presented in Figure 8. During MY 34 and the beginning of MY 35 ($L_s < 55^\circ$),
 632 InSight pressure measurements are lower compared to Viking 1 pressure by 5-10 Pa. de la
 633 Torre Juarez et al. (2019) also reported a pressure deficit at these times when studying
 634 the repeatability of MSL pressure data. Using MCS thermal data, they relate this to a
 635 possible increase of the NSPC expansion during MY 34 compared to MY 33. Such an
 636 expansion would consequently decrease the atmospheric mass at this time, reduce the
 637 surface pressure, and thereby explain the deficit observed. This deficit is not observed
 638 during Northern winter of MY 35 with MSL and InSight pressure data, and thus can-
 639 not be linked to a secular change.

640 After the sublimation of the NSPC during MY 35, the InSight pressure measure-
 641 ments match Viking pressures very well within the uncertainties associated with the in-
 642 terpolation method. The weather-induced uncertainty might explain the small deficit of
 643 pressure ($\sim 2\text{-}3$ Pa) observed at $L_s > 250^\circ$ because Viking 1 pressure was more affected
 644 by baroclinic activity as the lander is at a higher latitude than InSight. There is also less
 645 confidence in the Viking 1 pressure average during this period, as a lot of the measure-
 646 ments available at this time of the year were affected by the first global dust storm recorded
 647 by Viking (Ryan & Sharman, 1981), and thus removed from the dataset.

648 However, the overall strong agreement between Viking 1 interpolated surface pres-
 649 sure and InSight thermally corrected measurements strongly supports the assumption
 650 that the atmospheric mass has not changed since the Viking era, nearly forty Earth years

651 before the InSight era. More precisely, the comparison between InSight and Viking 1 pres-
652 sure data suggests that the atmospheric mass has not changed by more than $\pm 7\text{--}8$ Pa,
653 knowing that our method has an accuracy of ~ 11 Pa at $3\text{-}\sigma$. Our results suggest that
654 SPRC mass balances from Malin et al. (2001); Blackburn et al. (2010) might have been
655 overestimated, but support low estimated values of atmospheric mass gain/loss due to
656 the evolution of the SPRC (Thomas et al., 2016). Such results thus reinforce the assump-
657 tion that the SPRC does not suffer from major changes over decades, as indicated by
658 both imagery comparisons since the Mariner era and recent imagery dataset (Piqueux
659 & Christensen, 2008; Thomas et al., 2016). In fact, the SPRC might be varying with pe-
660 riods of erosion due to large summer dust events, followed by a period of deposition in
661 the next winter (Bonev et al., 2008; Becerra et al., 2015; Byrne et al., 2015; James et al.,
662 1992, 2010; Thomas et al., 2016). Further discussion on the role of dust events in the con-
663 densation and sublimation of CO_2 ice is shown in section 5.2. The possible influence of
664 CO_2 reservoirs under the SPRC on the durability of this cap has also been explored re-
665 cently (Buhler et al., 2020).

666 The strong agreement of the surface pressure comparison during the formation and
667 sublimation of seasonal caps (excluding the Northern winter of MY 34) also suggests a
668 low variability of the martian seasonal CO_2 cap dynamic. The interannual variability
669 of the recession of the seasonal polar cap has been widely studied in the literature (Benson
670 & James, 2005; Brown et al., 2010, 2012; Calvin et al., 2015, 2017; Giuranna et al., 2007;
671 James et al., 1979; James, 1979, 1982; James & Lumme, 1982; James et al., 1992; James
672 et al., 1996, 2000; James & Cantor, 2001; James et al., 2001; James et al., 2010; Kieffer
673 et al., 1972; Kieffer, 1979; Kieffer et al., 2000; Langevin et al., 2007; Piqueux et al.,
674 2015). The recession of the seasonal caps has been monitored through the optical prop-
675 erties of the CO_2 ice caps and albedo contrast with neighboring surfaces by Viking or-
676 biters (James et al., 1979; James, 1979, 1982; James & Lumme, 1982) and also completed
677 with telescopic observations (James et al., 1992). Further observations in the 90s/2000s
678 with the MOC camera on-board the Mars Global Surveyor orbiter (James et al., 2000;
679 James & Cantor, 2001; James et al., 2001; Benson & James, 2005) and telescopic obser-
680 vations (James et al., 1996) have shown good repeatability in the recession curves, de-
681 spite some local differences. This similarity in the retreat of the seasonal caps has also
682 been confirmed with spectroscopic studies (Langevin et al., 2007; Brown et al., 2010) but
683 their observations have limited coverage. More recently, Calvin et al. (2015, 2017) have
684 shown, using MARCI images taken recently (MY 28-31), that the retreat of the seasonal
685 caps was globally similar to the ones observed by Viking, even if some discrepancies ap-
686 pear at discrete locations. However, exploiting these observations has been impeded by
687 the challenging illumination conditions of the polar caps during the recession periods (see
688 Piqueux et al. (2015) for a complete review of these issues). To counterbalance these lim-
689 itations in the visible, the retreat of the seasonal caps has also been studied by thermal
690 measurements in the infrared. The first observations were made by Viking (Kieffer et
691 al., 1972; Kieffer, 1979) and the most recent studies (Kieffer et al., 2000; Giuranna et al.,
692 2007; Piqueux et al., 2015) have again shown high repeatability in the retreat time-lapse
693 of the seasonal ice caps. Small interannual variabilities exist but are mainly linked to the
694 influence of global dust storms (Piqueux et al., 2015; Calvin et al., 2015, 2017) (see sec-
695 tion 5.2 for a discussion on this topic).

696 Here, the good agreement between the InSight and Viking surface pressure (Fig-
697 ure 8) during the formation and sublimation of seasonal caps during MY 35 also con-
698 firms the good repeatability in the recession of the polar caps between the Viking pe-
699 riod and present. This result is contrary to a faster retreat of the SSPC that could be
700 assumed when looking at Figure 2a. Indeed, the large difference in pressure observed in
701 Figure 2a) (~ 20 Pa) would imply a lower extent of the SSPC when comparing SSPC
702 observed during the Viking period and today. To further refute the possible faster re-
703 treat of the SSPC (and thus validate again our correction), as well as the good agree-
704 ment between Viking's observations of the SSPC retreat with today's observations, we

705 propose in the following a comparison of the caps' albedo taken at these two periods. To
 706 do so, we exploit images of the SSPC taken by Viking Orbiter 2 during MY 12 (James
 707 et al., 1979) and MARCI images (Malin et al., 2001) taken during MY 35 (images from
 708 MY 34 are not used because of the global dust storm that occurred during this year, hin-
 709 dering the visual detection of the caps). Piqueux et al. (2015) noted interannual vari-
 710 ability in the caps' dynamics due to global dust storms. We thus add MY 33 to the com-
 711 parison as a control year in case the global dust storm at the end of MY 34 influenced
 712 the cap dynamics during MY 35. Furthermore, even if the cap boundary is composed
 713 of water ice after the sublimation of the seasonal CO₂ ice (see the spectroscopic study
 714 in Langevin et al. (2007)), we assume that the albedo comparison between the Viking
 715 decade and late 2010s/early 2020s also reflects possible changes in the CO₂ cycle and
 716 the sublimation of the SSPC.

717 Details on the composition of MARCI polar mosaic are given in Calvin et al. (2015,
 718 2017). We select $L_s = 192.6^\circ$ for the comparison as Viking mosaic is available at this time
 719 (Figure 5 of James et al. (1979)) and as InSight uncorrected pressure data present a large
 720 difference with Viking 1 pressure data at this time of the year (Figure 2a). Similar anal-
 721 ysis and conclusions can be drawn using other L_s (not shown here). The comparisons
 722 are presented in Figure 9. On Viking images, we flag with blue arrows craters or easily
 723 distinguishable topographies that are covered by ice at the boundary of the cap. We then
 724 look at MARCI images to see if the element is still covered by ice at the same time of
 725 the year. In this case, the element is flagged by a green arrow, whereas in the case of a
 726 divergence with Viking observations, the element is flagged by a red arrow. In case of
 727 doubt about the presence of ice, we flag the crater with an orange arrow. The compar-
 728 isons (Figure 9) underline that no major changes have happened in the dynamic of the
 729 seasonal caps as the same extend of CO₂ ice is observed. It thus confirms what has been
 730 observed by comparing Viking 1 and InSight pressure data. The good agreement between
 731 these observations refutes the possibility of a discrepancy in atmospheric mass between
 732 Viking and InSight during the sublimation of the SSPC. It also reinforces the credibil-
 733 ity of our correction, as the Viking and InSight pressure curves match well after the re-
 734 calibration. Little variability can be noted as revealed by the orange arrows. It can be
 735 explained by some observational biases. First, MARCI mosaics are built with images taken
 736 during all the day, and at different LTST. Hence, some ice might have sublimated dur-
 737 ing the day and would not be present on the mosaic. Second, the discrepancies on Fig-
 738 ure 9f are actually a consequence of the timing of the mosaic, as the images are not taken
 739 exactly at the same L_s and illumination conditions. At least, it is very unlikely that these
 740 discrepancies observed are due to a faster retreat of the seasonal cap as a consequence
 741 of the MY 34 global dust storm. Our GCM simulations show indeed that this retreat
 742 should occur at the same speed between MY 33 and 35. Finally, we acknowledge that
 743 this comparison is limited as we are looking at specific topographic features to compare
 744 the SSPC observed by Viking and InSight. Future analysis using MARCI observations
 745 should make a more complete study of the SSPC boundaries (like Calvin et al. (2017)
 746 for instance) to definitively conclude on the good agreement between Viking 2 orbiter
 747 and MARCI images of the SSPC.

748 Thus, the comparison between Viking 1 and InSight pressure data, as well as the
 749 preliminary comparison of images taken by the Viking 2 orbiter and the MARCI cam-
 750 era during MY 35 suggest the absence of secular pressure changes or modifications in
 751 the dynamics of the seasonal ice caps.

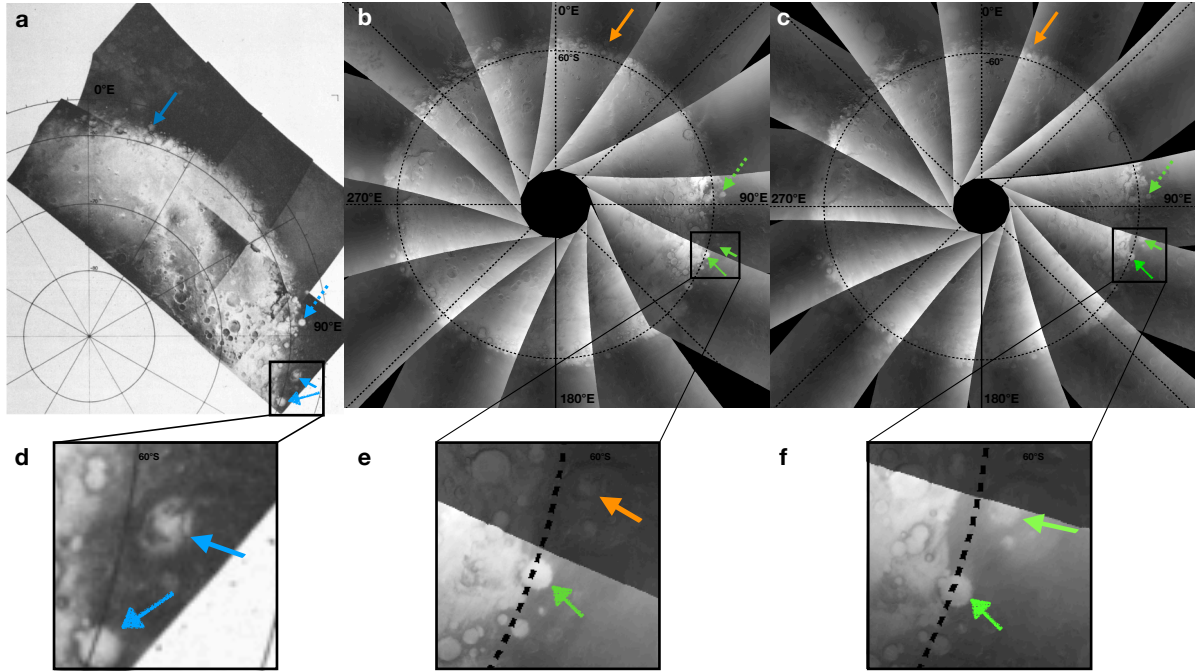


Figure 9. Comparison of the SPPC images taken by (a) Viking orbiter during MY 12, $L_s = 192.6^\circ$ (extracted from James et al. (1979)); (b) MARCI during MY 33, $L_s = 192.3^\circ$; and (c) MARCI during MY 35, $L_s = 192.9^\circ$. Blue arrows flag characteristic surface features for the comparison like craters. Orange arrows indicate a possible difference between the Viking images and MARCI images while green arrows indicate a good match between the images. d) to f) are zoom on the lowest flagged craters of a), b), c). The 60°S circle of latitude on image d) extracted from James et al. (1979) is misplaced, but arrows point to the same elements.

752 5 Discussion

753 5.1 Evolution of the atmospheric mass since MY 29

754 The non-detection of atmospheric mass changes between the 1970s and present dis-
 755 agrees with the conclusions obtained from the comparison between Viking and Phoenix
 756 surface pressure made in (Haberle & Kahre, 2010). The preliminary comparison between
 757 MSL and Viking 2 pressure data, which are nearly at the same altitude above the sur-
 758 face, did not show any significant increase of the atmospheric mass, but rather possibly
 759 a small decrease. We propose to extend this analysis by also comparing Phoenix and MSL
 760 data with Viking 1 pressures, using our methodology presented in section 5.1 for the
 761 comparison between Viking 1 and InSight pressure. Phoenix data used here are extracted
 762 from Taylor et al. (2010), as they are thus corrected from the temperature gradient within
 763 the sensor that disturbed the measurements (Taylor et al., 2010). The results are pre-
 764 sented in Figure 10.

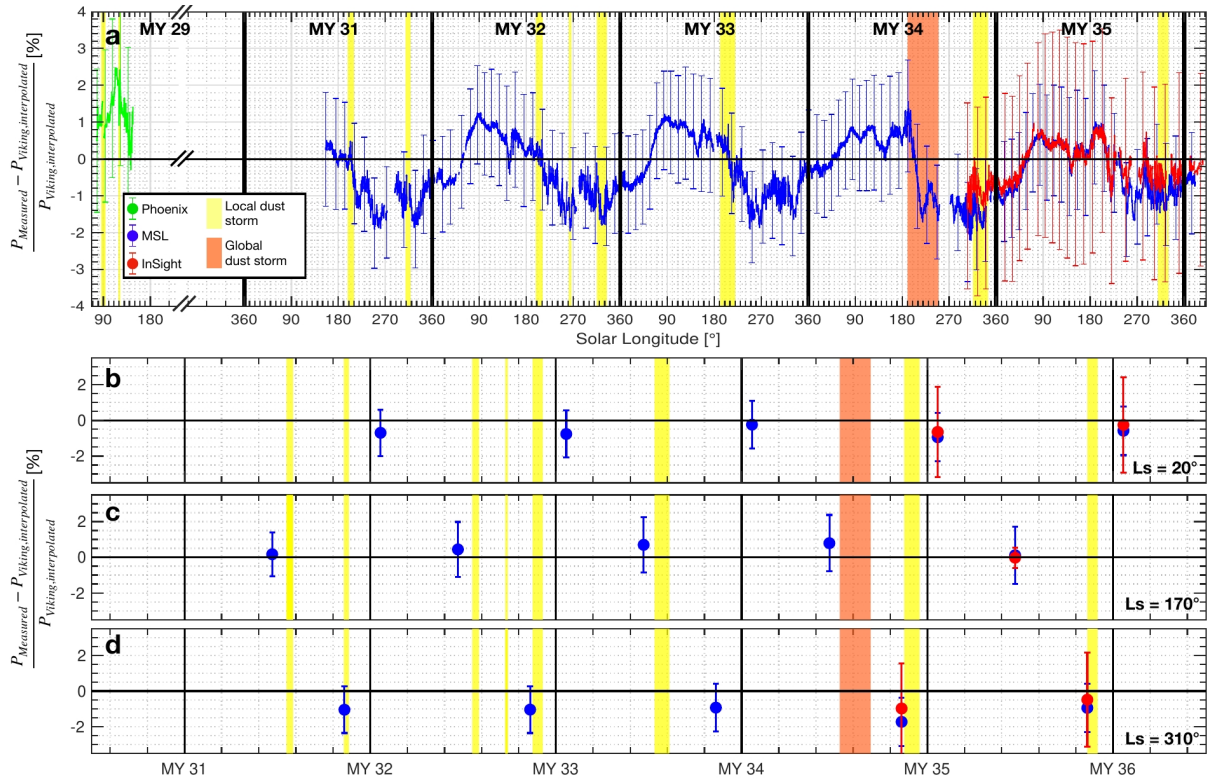


Figure 10. a) Comparison of the surface pressure measured by Phoenix (green dots), MSL (blue dots), and InSight (red dots), to Viking 1 measurements (interpolated at each landing sites), from MY 29 to MY 36. Yellow boxes correspond to periods of local dust storms at landing sites (Holstein-Rathlou et al., 2010; Ordonez-Etxeberria et al., 2019), while the orange box corresponds to the period of MY 34 global dust storm (Viúdez-Moreiras et al., 2019; Lemmon et al., 2019). b) to d) Evolution of the relative difference between Viking 1 interpolated and MSL (blue) and InSight (red), as a function of martian year at $L_s = 20^\circ$ (b), $L_s = 170^\circ$ (c), $L_s = 310^\circ$ (d). The error bars indicate the sensitivity of the comparison with regards to the interpolation uncertainty at $3\text{-}\sigma$, as described in 2.2.

765 Figure 10a underlines an excess of pressure when comparing Phoenix measurements
 766 to Viking 1 interpolated to Phoenix landing site. Such result is consistent with the anal-
 767 ysis from Haberle and Kahre (2010). However, the location of Phoenix must be consid-
 768 ered and might qualify their conclusions. Phoenix landed at a high latitude (68.22°N)
 769 compared to the other measurements used in this study that were made at mid/equatorial
 770 latitudes. This difference could lead to errors in our interpolation due to the large lat-
 771 itudinal pressure gradients. The error bars in Figure 10a underlines that the difference
 772 lies within the $3\text{-}\sigma$ uncertainty of our interpolation method. Hence, it is difficult to
 773 conclude on a possible increase of atmospheric mass in MY 29 using Phoenix measure-
 774 ments only. These observations might actually illustrate a real rise of the atmospheric mass
 775 due to a significant SPRC erosion during the MY 28 global dust storm (Montabone et al.,
 776 2015). Bonev et al. (2008); Becerra et al. (2015); Byrne et al. (2015); Thomas et al. (2016)
 777 report that southern spring/summer dust storms, like the one in MY 28, might enhance
 778 the SPRC sublimation, which would consequently increase the atmospheric mass. Fur-
 779 ther observations like an analysis of the SPRC extent between MY 27, 28, 29 should help
 780 to find the explanation of this increase of the surface pressure at the Phoenix land-
 781 ing site.

782 The comparisons of MSL and InSight data with Viking 1 pressure measurements
 783 both show the same results, i.e., an excess of pressure for $90^\circ < L_s < 180^\circ$, and a deficit
 784 elsewhere. Such divergences are small (less than 1% generally) and both comparisons
 785 are consistent, i.e., MSL and InSight present a deficit or excess of pressure at the same
 786 time of the year, but MSL data have sometimes larger relative differences. We note a
 787 repeatable annual cycle in Fig. 10a but this is actually a small systematic and seasonal
 788 error in the estimation by the GCM of the meteorological component of the pressure cy-
 789 cle (Hourdin et al., 1993). We study with Figures 10b to d the evolution of these diver-
 790 gences to Viking interpolated pressure, at three times of the year: $L_s = 20^\circ, 170^\circ, 310^\circ$.
 791 No clear trend can be established when comparing MSL or InSight to Viking 1 pressure
 792 data, thus rejecting the idea of a monotonic SPRC mass balance over the years. The pos-
 793 sibility of an erosion of the SPRC following the storm in MY 34 is difficult to show from
 794 the pressure data. First, the pressure recorded by MSL at the end of MY 34 was strongly
 795 impacted by a local dust storm (Viúdez-Moreiras et al., 2020). Moreover, when the storm
 796 stopped, the northern seasonal cap was still forming, with potentially an anomalous ex-
 797 tent that lead to a decrease in the available atmospheric mass (de la Torre Juarez et al.,
 798 2019). The uncertainty in both the data and the interpolation, represented by the er-
 799 ror bars in Figure 10, also explain the deficit observed by InSight and MSL. These two
 800 comparisons suggest again that there is no significant long-term pressure change.

801 5.2 CO₂ cycle and dust

802 What can induce year-to-year variations in the seasonal CO₂ ice budget? As re-
 803 viewed in Titus et al. (2017), the CO₂ ice condensation and sublimation rates are con-
 804 trolled by the local energy balance, as the CO₂ condenses or sublimates in the exact amount
 805 needed to keep the surface and atmosphere at the CO₂ condensation temperature when
 806 ice is present.

807 At a given season, this energy balance could fluctuate from one year to the other.
 808 This stems from interannual changes in both CO₂ ice albedo and emissivity, as well as
 809 changes in the incident infrared radiation due to variations in the heat advected by the
 810 atmosphere or by the clouds. It is also sensitive to the amount of heat stored in the sub-
 811 surface during previous seasons: the heat conducted from the subsurface up to the CO₂
 812 ice on the surface depends on the subsurface temperatures, which are themselves influ-
 813 enced by the temperature from the previous summer when no CO₂ ice was present.

814 On these grounds, atmospheric dust can influence the CO₂ budget in a variety of
 815 ways:

816 Firstly, during the condensation phase (i.e. in the polar night), dust primarily in-
 817 creases the thermal emissivity of the atmosphere and thus its radiative cooling (Pollack
 818 et al., 1990). More CO₂ condenses in the atmosphere and less on the surface. The net
 819 effect is an observed decrease of the thermal infrared emission at the top of the atmo-
 820 sphere due to the radiative effect of CO₂ clouds and/or the lower emissivity of the CO₂
 821 snow freshly deposited from the atmosphere (Forget & Pollack, 1996; Cornwall & Titus,
 822 2009). This means less CO₂ ice condensing during a dust storm reaching the polar night.
 823 CO₂ ice deposits that condensed in the presence of extra dust may also be durably mod-
 824 ified. They could have a higher albedo because they were formed from larger fractions
 825 of small particles condensed in the atmosphere, but their albedo could also be lowered
 826 by the contamination of more dust particles. Which effects dominate? Looking at the
 827 seasonal deposits around the north pole, Byrne et al. (2008) found that the northern fall
 828 2001 global dust-storm resulted in slightly brighter ice deposits in the following spring.
 829 They considered this result to be "counter-intuitive". It can probably be attributed to
 830 comparatively more atmospheric condensation in fall enhancing the spring albedo. The
 831 amount of airborne dust also influences the atmospheric circulation and thus the trans-
 832 port of heat and the dilution of non-condensable gas, these last ones influencing the CO₂

833 condensation temperature (Forget et al., 2008; Piqueux et al., 2020). Airborne dust can
834 impact the structure of the polar vortices (Ball et al., 2021; Guzewich et al., 2016; Streeter
835 et al., 2021), possibly inducing a warming of the Northern polar vortex (Guzewich et al.,
836 2016)) that can affect the CO₂ condensation rate (Zhao et al., 2021). Conversely, the ac-
837 celeration of the meridional wind speed induced by an increase of dust loading can lead
838 to an acceleration of the northern CO₂ condensation process (Zhao et al., 2021). All of
839 these possible modifications of the atmospheric dynamic and their impact on the CO₂
840 ice budget are however sensitive to the timing of the dust loading (Zhao et al., 2021).

841 Secondly, during the sublimation phase, or more generally when CO₂ ice is signif-
842 icantly sunlit, the net effect of airborne dust is also equivocal, as studied by Bonev (2002);
843 Bonev et al. (2008). Airborne dust redistributes the downward radiation from solar to
844 thermal infrared because dust absorbs solar radiations and re-emits at thermal wavelengths.
845 Model calculation and camera observations show that regions of high-albedo CO₂ frost
846 will sublimate faster with more airborne dust (as they mostly absorb in the thermal range)
847 whereas low-albedo regions will sublimate slower (as they mostly absorb in the visible)
848 (Bonev et al., 2003; Bonev et al., 2008).

849 Thirdly, during summer (when no CO₂ ice is present) airborne dust could also mod-
850 ify the mean surface temperature at high latitude and the stored subsurface heat, but
851 once again the net effect is subtle and depends on the atmospheric temperatures and sur-
852 face albedo.

853 Overall, determining the net effect of regional and global dust storms on the sea-
854 sonal CO₂ cycle is not straightforward as the different processes involved could tend to
855 balance each other. This may explain why the seasonal cycle was observed to be rel-
856 atively insensitive to the occurrence or non-occurrence of global dust storms in the multi-
857 year Viking Lander pressure records (James et al., 1992). Now the InSight pressure mea-
858 surements suggest that the Northern seasonal polar cap was slightly and unusually more
859 massive during the winter and spring of MY 34 (after $L_s = 300^\circ$) following an unusual
860 global dust storm that occurred throughout the preceding autumn, well before the ob-
861 served effect on the seasonal ice cap, in accordance with the observations from MSL (de la
862 Torre Juarez et al., 2019). Based on the discussion above, we can speculate that the most
863 likely reason for this small excess of mass could be due to a slight increase of the ice albedo,
864 resulting from more atmospheric condensation during fall. An alternative explanation
865 could invoke the fact that the post-storm winter atmosphere in the polar night could be
866 slightly depleted in airborne dust and/or ice clouds compared to regular years, reduc-
867 ing the fraction of CO₂ ice clouds and snowfall and therefore increasing the polar night
868 thermal infrared cooling to space, and thus the net condensation rate.

869 In theory, these hypotheses could be tested using climate simulations performed
870 with a GCM. The current version of the LMD GCM can account for the effect of dust
871 on the atmospheric dynamics and radiative cooling as well as their consequence on the
872 atmospheric CO₂ condensation and its effect on the polar night emissivity (Forget et al.,
873 1998). However, because of the lack of dust observations in the polar night, the dust cli-
874 matology available to simulate MY 34 (Montabone et al., 2020) in the polar regions is
875 probably not adequate to represent well what happened (either during or after the dust
876 storm). Furthermore, the GCM does not include any feedback on the CO₂ ice deposit
877 albedo, which cannot be affected by dust storm (neither the albedo increase due to the
878 additional atmospheric condensation or decrease by the additional dust contamination).
879 Nevertheless, we performed GCM simulations using the MY 34 and MY 35 dust scenar-
880 ios (Montabone et al., 2015), looking for other differences that could result from the MY 34
881 global dust storm. The simulated CO₂ mass cycles in the two years were found to be al-
882 most almost identical (not shown), confirming that processes that are well represented
883 in the GCM (e.g. atmospheric dynamic and heat transport, non-condensable gas enrich-
884 ment) are probably not involved in the interannual seasonal cap variations observed by
885 InSight.

886 **6 Conclusions**

887 In this study, we track long-term pressure changes on Mars by comparing for the
 888 first time the InSight and Viking pressure data. We extend this comparison to other pres-
 889 sure data that have been at the surface of Mars over the last 40 years. The main con-
 890 clusions of this investigation are:

- 891 • InSight pressure measurements have an unexpected thermal sensitivity to sensor
 892 temperature, which dramatically impacts the recorded annual pressure and makes
 893 its evolution inconsistent over the two years of the mission.
- 894 • A polynomial correction in the sensor temperature is proposed, using a ratio of
 895 MSL pressure data to account for the interannual variability of the seasonal pres-
 896 sure cycle, observed by MSL between the beginning of MY 34 and 35. For pos-
 897 itive sensor temperature, the correction removes between 1 and 5 Pa to the raw
 898 pressure measurements, while it can adds between 1 to 15 Pa for negative sensor
 899 temperature.
- 900 • InSight data, once recalibrated, have an uncertainty of 1.7 to 2.3 Pa at $1\text{-}\sigma$ com-
 901 pared to the initial uncertainty of 1.5 Pa at $1\text{-}\sigma$. The correction does not lead to
 902 a major uncertainty compromising the detection of secular pressure changes com-
 903 pared to the Viking data, or of interannual changes.
- 904 • The comparison between MSL and InSight pressure during MY 34 and 35 rein-
 905 forces the credibility of our correction. This comparison also highlights a pressure
 906 deficit at the MSL site at $L_s \sim 270^\circ$. This deficit could be induced by a change in
 907 the scale height due to a significant amount of dust within Gale Crater, creating
 908 a hot atmospheric layer in the local near-surface atmosphere.
- 909 • We design two high-accuracy methods for pressure interpolation, at local and global
 910 scales, that correct the effects of local and large-scale atmospheric circulations as
 911 well as the martian orography on the seasonal pressure variations. Both methods
 912 use a scale height computed with the air temperature at an altitude of 1 km. The
 913 influence of atmospheric parameters on this interpolation was quantified at 1% of
 914 the absolute pressure at a $3\text{-}\sigma$ level.
- 915 • The Viking 1 and InSight pressure comparison does not show significant secular
 916 pressure change, as previously postulated with the Viking and Phoenix compar-
 917 ison. Our results show that the atmospheric mass has not changed by more than
 918 $\pm 7 - 8$ Pa, knowing that our method has an accuracy of ~ 11 Pa at $3\text{-}\sigma$. This
 919 suggests that either the sublimation of the SPRC is much slower than expected,
 920 or that the system is actually in equilibrium. In any case, it appears that the mass
 921 balance computations that predicted a very large increase in atmospheric mass
 922 or the rapid SPRC disappearance are overestimated.
- 923 • Similarly, a first visual comparative analysis of Viking 2 orbiter and MARCI im-
 924 ages of the seasonal ice caps does not show significant change in the dynamics of
 925 the seasonal ice caps, as observed when comparing the annual variations of the
 926 ice caps with pressure data. This comparison requires to be completed with more
 927 observations during MY 35 to compute the exact recession curve and compare it
 928 with Viking observations.
- 929 • Both of these conclusions are also supported by the comparison between MSL and
 930 Viking 1 pressure data. Using the five martian years of MSL pressure records, we
 931 cannot establish a secular trend.
- 932 • Phoenix surface pressure data might highlight an increase of the atmospheric mass
 933 during MY 29, suggesting a possible erosion of the SPRC after the MY 28 global
 934 dust storm. Analysis of the SPRC boundary during MY 27, 28, and 29 would help
 935 to study this assumption.
- 936 • The NSPC is more extended during MY 34 compared to MY 35. However, the
 937 physical mechanisms that explain this extent are not understood yet. Investiga-

938 tions conducted with the LMD GCM suggest that atmospheric dynamics, heat trans-
 939 port, or non-condensable gas enrichment are not at the origin of this phenomenon.

940 The Perseverance rover that arrived on Mars on February 18th, 2021 at a latitude
 941 close to Viking 1 lander will provide a unique new pressure dataset to contribute to the
 942 study of interannual and secular pressure changes. Cross-analyses between SPRC evo-
 943 lution, dust storms, and atmospheric mass measurements would also help to better un-
 944 derstand the evolution of the SPRC and its relative balance.

945 **Appendix A Impact of MSL pressure uncertainties on InSight pres-** 946 **sure correction**

947 We apply the propagation of uncertainty on the definition of β (Eq. 6):

$$\frac{\sigma_\beta}{\beta} = \sqrt{\left(\frac{\sigma_{P_{\text{MSL},Y_1}}}{P_{\text{MSL},Y_1}}\right)^2 + \left(\frac{\sigma_{P_{\text{MSL},Y_2}}}{P_{\text{MSL},Y_2}}\right)^2 - 2\frac{\text{Cov}(P_{\text{MSL},Y_1}, P_{\text{MSL},Y_2})}{P_{\text{MSL},Y_1}P_{\text{MSL},Y_2}}} \quad (\text{A1})$$

948 where $\text{Cov}(P_{\text{MSL},Y_1}, P_{\text{MSL},Y_2})$ is the covariance between measurements P_{MSL,Y_1} and
 949 P_{MSL,Y_2} .

950 Let us assume that:

$$P_{\text{MSL},Y_1} = P_{\text{MSL}}(t_{Y1}) = P_{\text{atm,true}}(t_{Y1}) + \epsilon(t_{Y1}) + \delta(t_{Y1}) \quad (\text{A2})$$

$$P_{\text{MSL},Y_2} = P_{\text{MSL}}(t_{Y2}) = P_{\text{atm,true}}(t_{Y2}) + \epsilon(t_{Y2}) + \delta(t_{Y2}) \quad (\text{A3})$$

951 with

- 952 • $P_{\text{atm,true}}(t)$ the true atmospheric pressure that MSL should have recorded with-
 953 out any error
- 954 • $\epsilon(t)$ the error on a measurement due to:
 - 955 – The error on the absolute measurement due to the initial calibration, estimated
 956 to be at most 4 Pa at $3\text{-}\sigma$ over the possible pressure range at the MSL landing
 957 site (Harri et al., 2014).
 - 958 – The error due to elevation change. During the period considered here, the alti-
 959 tude of the rover changed by nearly 100 m, which could lead to a change in
 960 pressure of 8 Pa at $3\text{-}\sigma$.
 - 961 – At least, the estimated error is $\sqrt{8^2 + 4^2} \approx 9$ Pa at $3\text{-}\sigma$
 - 962 – Since 15-day averaged data are used, the uncertainty related to the precision
 963 of the measurements is assumed to be negligible.
- 964 • $\delta(t)$, the drift error which theoretically evolves at a rate of 1 Pa/MY at $3\text{-}\sigma$ (Harri
 965 et al., 2014).

966 We model these errors by random variables whose variance is given by the previ-
 967 ous values. The last two terms in the expression of P_{MSL} , thus representing the error on
 968 the measurement, are random variables of variance. We introduce $\sigma_{P_{\text{MSL}}} = \sqrt{\sigma_\epsilon^2 + \sigma_\delta^2}$
 969 by independence of these two terms.

970 Since the errors are computed over the range of possible values of the MSL mea-
 971 surements and not a precise value, the errors ϵ, δ are independent of $P_{\text{atm,true}}$. Moreover,
 972 the $P_{\text{atm,true}}$ between the two years are completely independent. Using the bilinearity
 973 of the covariance, and these independences, we obtain:

$$Cov(P_{MSL,Y1}, P_{MSL,Y2}) = Cov(\epsilon(t_{Y1}), \epsilon(t_{Y2})) + Cov(\delta(t_{Y1}), \delta(t_{Y2})) \quad (A4)$$

974 By definition, for two random variables a, b :

$$Cov(a, b) = \rho(a, b)\sigma_a\sigma_b \quad (A5)$$

975 with ρ the correlation coefficient. ϵ has been determined during calibration tests
976 and is assumed to be constant over the mission, so that

$$Cov(\epsilon(t_{Y1}), \epsilon(t_{Y2})) = \sigma_\epsilon^2 \quad (A6)$$

977 Assuming that the drift grows at a rate of 1 Pa/MY, we have:

$$Cov(\delta(t_{Y1}), \delta(t_{Y2})) = Cov(\delta(t_{Y1}), \delta(t_{Y1}) + 1) = Cov(\delta(t_{Y1}), \delta(t_{Y1})) \quad (A7)$$

by property of the covariance. We thus have:

$$Cov(\delta(t_{Y1}), \delta(t_{Y2})) = \sigma_\delta^2 \quad (A8)$$

978 Hence, Eq. A4 becomes:

$$\frac{\sigma_\beta}{\beta} = \sigma_{P_{MSL}} \sqrt{\left(\frac{1}{P_{MSL,Y1}} - \frac{1}{P_{MSL,Y2}}\right)^2} \quad (A9)$$

which gives:

$$\frac{\sigma_\beta}{\beta} \sim 5 \times 10^{-5} \quad (A10)$$

979 Open Research

980 InSight pressure uncorrected data can be retrieved from the PDS (Banfield, 2019),
981 MSL REMS and Viking 1 pressure data can be retrieved from the PDS (Gomez-Elvira,
982 2019; Tillman, 1989). Phoenix corrected data are given with Taylor et al. (2010). MARCI
983 mosaics can be reconstructed from the images that can be retrieved from the PDS (Malin,
984 2007). THEMIS images can be retrieved from the PDS (Christensen, 2002). The Mars
985 Climate Database can be retrieved upon request (see [http://www-mars.lmd.jussieu](http://www-mars.lmd.jussieu.fr/mars/access.html)
986 [.fr/mars/access.html](http://www-mars.lmd.jussieu.fr/mars/access.html)).

987 Data files for figures used in this analysis are available in a public repository, see
988 Lange et al. (2022).

989 Acknowledgments

990 This project has received funding from the European Research Council (ERC) under the
991 European Union's Horizon 2020 research and innovation program (grant agreement No
992 835275). This work was performed using HPC computing resources from GENCI-CINES
993 (Grant 2021-A0100110391). All co-authors acknowledge NASA, the Centre National d'Études
994 Spatiales (CNES) and its partner agencies and institutions, and the flight operations team
995 at JPL, CAB, SISMOC, MSDS, IRIS-DMC, and PDS for providing InSight data. The
996 members of the InSight engineering and operations teams are warmly acknowledged for
997 their dedication and hard work in allowing InSight to perform the numerous measure-
998 ments used in this study. LL and all French co-authors acknowledge support from the

999 CNES. Part of this work was performed at the Jet Propulsion Laboratory, California In-
 1000 stitute of Technology, under a contract with NASA. This study is InSight Contribution
 1001 Number 248.

1002 References

- 1003 Ball, E. R., Mitchell, D. M., Seviour, W. J. M., Thomson, S. I., & Vallis, G. K.
 1004 (2021). The roles of latent heating and dust in the structure and variability of
 1005 the northern martian polar vortex. *The Planetary Science Journal*, 2(5), 203.
 1006 doi: 10.3847/psj/ac1ba2
- 1007 Banerdt, W. B., Smrekar, S. E., Banfield, D., Giardini, D., Golombek, M., Johnson,
 1008 C. L., ... Wieczorek, M. (2020). Initial results from the insight mission on
 1009 Mars. *Nature Geoscience*, 13(3), 183-189. doi: 10.1038/s41561-020-0544-y
- 1010 Banfield, D. (2019). *InSight APSS PS Data Product Bundle*. NASA Planetary Data
 1011 Systeme. doi: 10.17189/1518939
- 1012 Banfield, D., Rodriguez-Manfredi, J. A., Russell, C. T., Rowe, K. M., Leneman, D.,
 1013 Lai, H. R., ... Team, T. T. (2019). Insight auxiliary payload sensor suite
 1014 (APSS). *Space Science Reviews*, 215(1), 4. doi: 10.1007/s11214-018-0570-x
- 1015 Banfield, D., Spiga, A., Newman, C., Forget, F., Lemmon, M., Lorenz, R., ...
 1016 Banerdt, W. B. (2020). The atmosphere of Mars as observed by InSight.
 1017 *Nature Geoscience*, 13(3), 190-198. doi: 10.1038/s41561-020-0534-0
- 1018 Barnes, J. R. (1980). Time spectral analysis of midlatitude disturbances in the mar-
 1019 tian atmosphere. *Journal of Atmospheric Sciences*, 37(9), 2002 - 2015. doi: 10
 1020 .1175/1520-0469(1980)037<2002:TSAOMD>2.0.CO;2
- 1021 Becerra, P., Byrne, S., & Brown, A. J. (2015). Transient bright “halos” on the south
 1022 polar residual cap of Mars: Implications for mass-balance. *Icarus*, 251, 211–
 1023 225. doi: 10.1016/j.icarus.2014.04.050
- 1024 Benson, J. L., & James, P. B. (2005). Yearly comparisons of the martian polar caps:
 1025 1999–2003 Mars orbiter camera observations. *Icarus*, 174(2), 513-523. (Mars
 1026 Polar Science III) doi: 10.1016/j.icarus.2004.08.025
- 1027 Blackburn, D. G., Bryson, K. L., Chevrier, V. F., Roe, L. A., & White, K. F.
 1028 (2010). Sublimation kinetics of co2 ice on Mars. *Planetary and Space Sci-*
 1029 *ence*, 58(5), 780-791. doi: 10.1016/j.pss.2009.12.004
- 1030 Bonev, B. P. (2002). Regression of the mountains of mitchel polar ice after the onset
 1031 of a global dust storm on Mars. *Geophysical Research Letters*, 29(21). doi: 10
 1032 .1029/2002gl015458
- 1033 Bonev, B. P., Hansen, G. B., Glenar, D. A., James, P. B., & Bjorkman, J. E. (2008).
 1034 Albedo models for the residual south polar cap on Mars: Implications for the
 1035 stability of the cap under near-perihelion global dust storm conditions. *Plane-*
 1036 *tary and Space Science*, 56(2), 181-193. (Mars Polar Processes: Atmosphere-
 1037 Surface Interactions) doi: 10.1016/j.pss.2007.08.003
- 1038 Bonev, B. P., James, P. B., Bjorkman, J. E., Hansen, G. B., & Wolff, M. J. (2003).
 1039 Effects of Atmospheric and Surface Dust on the Sublimation Rates of CO2 on
 1040 Mars. In S. Clifford, P. Doran, D. Fisher, & C. Herd (Eds.), *Third interna-*
 1041 *tional conference on Mars polar science and exploration* (p. 8052).
- 1042 Brown, A. J., Calvin, W. M., McGuire, P. C., & Murchie, S. L. (2010). Compact
 1043 reconnaissance imaging spectrometer for Mars (crism) south polar mapping:
 1044 First Mars year of observations. *Journal of Geophysical Research: Planets*,
 1045 115(E2). doi: 10.1029/2009JE003333
- 1046 Brown, A. J., Calvin, W. M., & Murchie, S. L. (2012). Compact reconnaissance
 1047 imaging spectrometer for Mars (crism) north polar springtime recession map-
 1048 ping: First 3 Mars years of observations. *Journal of Geophysical Research:*
 1049 *Planets*, 117(E12). doi: 10.1029/2012JE004113
- 1050 Buhler, P. B., Ingersoll, A. P., Piqueux, S., Ehlmann, B. L., & Hayne, P. O. (2020).
 1051 Coevolution of Mars’s atmosphere and massive south polar CO2 ice deposit. ,

- 1052 4(4), 364–371. doi: 10.1038/s41550-019-0976-8
- 1053 Byrne, S., Hayne, P. O., Becerra, P., & HiRISE Team. (2015). Evolution and Sta-
1054 bility of the Residual CO₂ Ice Cap. In *Lunar and planetary science conference*
1055 (p. 1657).
- 1056 Byrne, S., Zuber, M. T., & Neumann, G. A. (2008). Interannual and seasonal behav-
1057 ior of Martian residual ice-cap albedo. , *56*(2), 194-211. doi: 10.1016/j.pss.2006
1058 .03.018
- 1059 Calvin, W., Cantor, B., & James, P. (2017). Interannual and seasonal changes in the
1060 south seasonal polar cap of Mars: Observations from my 28-31 using MARCI.
1061 *Icarus*, *292*, 144-153. doi: 10.1016/j.icarus.2017.01.010
- 1062 Calvin, W., James, P., Cantor, B., & Dixon, E. (2015). Interannual and sea-
1063 sonal changes in the north polar ice deposits of Mars: Observations from
1064 my 29–31 using MARCI. *Icarus*, *251*, 181-190. (Dynamic Mars) doi:
1065 10.1016/j.icarus.2014.08.026
- 1066 Chatain, A., Spiga, A., Banfield, D., Forget, F., & Murdoch, N. (2021). Seasonal
1067 variability of the daytime and nighttime atmospheric turbulence experienced
1068 by InSight on Mars. *Geophysical Research Letters*, *48*(22), e2021GL095453.
1069 (e2021GL095453 2021GL095453) doi: 10.1029/2021GL095453
- 1070 Christensen, P. (2002). *Odyssey themis vis geo v2.0*. NASA Planetary Data System.
1071 doi: 10.17189/1520386
- 1072 Christensen, P. R., Jakosky, B. M., Kieffer, H. H., Malin, M. C., Harry Y. McSween,
1073 J., Nealon, K., ... Ravine, M. (2004). The thermal emission imaging sys-
1074 tem (THEMIS) for the Mars 2001 Odissey mission. *Space Science Reviews*,
1075 *110*(1/2), 85–130. doi: 10.1023/b:spac.0000021008.16305.94
- 1076 Cornwall, C., & Titus, T. N. (2009). Spatial and temporal distributions of martian
1077 north polar cold spots before, during, and after the global dust storm of 2001.
1078 *Journal of Geophysical Research*, *114*(E2). doi: 10.1029/2008je003243
- 1079 de la Torre Juarez, M., Piqueux, S., Kass, D. M., Newman, C., & Guzewich, S. D.
1080 (2019). Pressure deficit in gale crater and a larger northern polar cap after
1081 the Mars year 34 global dust storm. In *Agu fall meeting abstracts* (Vol. 2019,
1082 p. P51C-02).
- 1083 Fonseca, R. M., Zorzano-Mier, M.-P., & Martín-Torres, J. (2018). Planetary bound-
1084 ary layer and circulation dynamics at Gale crater, Mars. *Icarus*, *302*, 537-559.
1085 doi: 10.1016/j.icarus.2017.11.036
- 1086 Forget, F., Hourdin, F., Fournier, R., Hourdin, C., Talagrand, O., Collins, M., ...
1087 Huot, J.-P. (1999). Improved general circulation models of the martian at-
1088 mosphere from the surface to above 80 km. *Journal of Geophysical Research:*
1089 *Planets*, *104*(E10), 24155-24175. doi: 10.1029/1999JE001025
- 1090 Forget, F., Hourdin, F., & Talagrand, O. (1998). Co₂ snowfall on Mars: Simulation
1091 with a general circulation model. *Icarus*, *131*(2), 302-316. doi: 10.1006/icar
1092 .1997.5874
- 1093 Forget, F., Millour, E., Montabone, L., & Lefevre, F. (2008). Non Condensable
1094 Gas Enrichment and Depletion in the Martian Polar Regions. In *Third inter-*
1095 *national workshop on the Mars atmosphere: Modeling and observations* (Vol.
1096 1447, p. 9106).
- 1097 Forget, F., & Pollack, J. B. (1996). Thermal infrared observations of the con-
1098 densing martian polar caps: CO₂ice temperatures and radiative budget.
1099 *Journal of Geophysical Research: Planets*, *101*(E7), 16865–16879. doi:
1100 10.1029/96je01077
- 1101 Forget, F., Spiga, A., Dolla, B., Vinatier, S., Melchiorri, R., Drossart, P., ...
1102 Gondet, B. (2007). Remote sensing of surface pressure on mars with the Mars
1103 Express/OMEGA spectrometer: 1. retrieval method. *Journal of Geophysical*
1104 *Research: Planets*, *112*(E8). doi: 10.1029/2006JE002871
- 1105 Giuranna, M., Formisano, V., Grassi, D., & Maturilli, A. (2007). Tracking the edge
1106 of the south seasonal polar cap of Mars. *Planetary and Space Science*, *55*(10),

- 1107 1319-1327. doi: doi.org/10.1016/j.pss.2006.12.005
- 1108 Golombek, M., Williams, N., Warner, N. H., Parker, T., Williams, M. G., Daubar,
1109 I., ... Sklyanskiy, E. (2020). Location and setting of the Mars InSight
1110 lander, instruments, and landing site. *Earth and Space Science*, 7(10),
1111 e2020EA001248. doi: 10.1029/2020EA001248
- 1112 Gomez-Elvira, J. (2019). *Mars science laboratory rover environmental monitoring*
1113 *station rdr data v1.0, modrdr v1.0*. NASA Planetary Data System. doi: 10
1114 .17189/1523033
- 1115 Guzewich, S. D., Newman, C. E., Smith, M. D., Moores, J. E., Smith, C. L., Moore,
1116 C., ... Battalio, M. (2017). The vertical dust profile over gale crater,
1117 Mars. *Journal of Geophysical Research: Planets*, 122(12), 2779-2792. doi:
1118 10.1002/2017je005420
- 1119 Guzewich, S. D., Toigo, A., & Waugh, D. (2016). The effect of dust on the martian
1120 polar vortices. *Icarus*, 278, 100-118. doi: 10.1016/j.icarus.2016.06.009
- 1121 Gómez-Elvira, J., Armiens, C., Carrasco, I., Genzer, M., Gómez, F., Haberle, R.,
1122 ... Zorzano, M.-P. (2014). Curiosity's rover environmental monitoring sta-
1123 tion: Overview of the first 100 sols. *Journal of Geophysical Research: Planets*,
1124 119(7), 1680-1688. doi: 10.1002/2013JE004576
- 1125 Haberle, R. M., Gómez-Elvira, J., de la Torre Juárez, M., Harri, A.-M.,
1126 Hollingsworth, J. L., Kahanpää, H., ... Teams, R. S. (2014). Preliminary
1127 interpretation of the rems pressure data from the first 100 sols of the MSL
1128 mission. *Journal of Geophysical Research: Planets*, 119(3), 440-453. doi:
1129 10.1002/2013JE004488
- 1130 Haberle, R. M., & Kahre, M. A. (2010). Detecting secular climate change on Mars.
1131 *International Journal of Mars Science and Exploration*, 4, 68-75. doi: 10.1555/
1132 mars.2010.0003
- 1133 Harri, A. M., Genzer, M., Kemppinen, O., Kahanpää, H., Gomez-Elvira, J.,
1134 Rodriguez-Manfredi, J. A., ... REMS/MSL Science Team (2014). Pres-
1135 sure observations by the Curiosity rover: Initial results. *Journal of Geophysical*
1136 *Research (Planets)*, 119(1), 82-92. doi: 10.1002/2013JE004423
- 1137 Hess, S. L., Henry, R. M., Leovy, C. B., Ryan, J. A., Tillman, J. E., Chamberlain,
1138 T. E., ... Mitchell, J. L. (1976). Preliminary meteorological results on Mars
1139 from the Viking 1 lander. *Science*, 193(4255), 788-791.
- 1140 Hess, S. L., Ryan, J. A., Tillman, J. E., Henry, R. M., & Leovy, C. B. (1980). The
1141 annual cycle of pressure on Mars measured by Viking landers 1 and 2. *Geo-*
1142 *physical Research Letters*, 7, 197-200.
- 1143 Holstein-Rathlou, C., Gunnlaugsson, H., Cantor, B., Ellehøj, M., Lange, C., Lem-
1144 mon, M., ... Smith, P. (2010). On dust storms observed at the Phoenix
1145 landing site.. (Conference date: 01-03-2010 Through 05-03-2010)
- 1146 Hourdin, F., Forget, F., & Talagrand, O. (1995). The sensitivity of the martian
1147 surface pressure and atmospheric mass budget to various parameters: A com-
1148 parison between numerical simulations and Viking observations. *Journal of*
1149 *Geophysical Research: Planets*, 100(E3), 5501-5523. doi: 10.1029/94JE03079
- 1150 Hourdin, F., Van, P. L., Forget, F., & Talagrand, O. (1993). Meteorological variabil-
1151 ity and the annual surface pressure cycle on Mars. *Journal of Atmospheric Sci-*
1152 *ences*, 50(21), 3625 - 3640. doi: 10.1175/1520-0469(1993)050<3625:MVATAS>
1153 2.0.CO;2
- 1154 Jakosky, B. M., & Haberle, R. M. (1990). Year-to-year instability of the Mars
1155 south polar cap. *Journal of Geophysical Research*, 95(B2), 1359. doi:
1156 10.1029/jb095ib02p01359
- 1157 James, P., Cantor, B., Malin, M., Edgett, K., Carr, M., Danielson, G., ... Vev-
1158 erka, J. (2000). The 1997 spring regression of the martian south polar
1159 cap: Mars orbiter camera observations. *Icarus*, 144(2), 410-418. doi:
1160 10.1006/icar.1999.6289
- 1161 James, P., Thomas, P., & Malin, M. (2010). Variability of the south polar cap of

- 1162 Mars in Mars Years 28 and 29. *Icarus*, 208(1), 82–85. doi: 10.1016/j.icarus
 1163 .2010.02.007
- 1164 James, P. B. (1979). Recession of martian north polar cap: 1977–1978 Viking ob-
 1165 servations. *Journal of Geophysical Research*, 84(B14), 8332. doi: 10.1029/
 1166 jb084ib14p08332
- 1167 James, P. B. (1982). Recession of martian north polar cap: 1979–1980 Viking obser-
 1168 vations. *Icarus*, 52(3), 565–569. doi: 10.1016/0019-1035(82)90016-1
- 1169 James, P. B., Briggs, G., Barnes, J., & Spruck, A. (1979). Seasonal recession of
 1170 Mars' south polar cap as seen by Viking. *Journal of Geophysical Research*,
 1171 84(B6), 2889. doi: 10.1029/jb084ib06p02889
- 1172 James, P. B., & Cantor, B. A. (2001, November). Martian North Polar Cap Reces-
 1173 sion: 2000 Mars Orbiter Camera Observations. , 154(1), 131-144. doi: 10.1006/
 1174 icar.2001.6653
- 1175 James, P. B., Cantor, B. A., & Davis, S. (2001). Mars orbiter camera observations
 1176 of the martian south polar cap in 1999–2000. *Journal of Geophysical Research:*
 1177 *Planets*, 106(E10), 23635-23652. doi: 10.1029/2000JE001313
- 1178 James, P. B., Clancy, R., Lee, S. W., Martin, L. J., & Bell, J. (1996). Seasonal re-
 1179 cession of martian south polar cap: 1992 hst observations. *Icarus*, 123(1), 87-
 1180 100. doi: 10.1006/icar.1996.0143
- 1181 James, P. B., Kieffer, H. H., & Paige, D. A. (1992). The seasonal cycle of carbon
 1182 dioxide on Mars. In M. George (Ed.), *Mars* (p. 934-968).
- 1183 James, P. B., & Lumme, K. (1982). Martian south polar cap boundary: 1971 and
 1184 1973 data. *Icarus*, 50(2-3), 368–380. doi: 10.1016/0019-1035(82)90130-0
- 1185 Kahanpää, H., Polkko, J., & Daly, M. (2021). Accuracy of the Phoenix and Viking
 1186 atmospheric pressure measurements: impact on detecting the climate change
 1187 on Mars.
 1188 doi: 10.5194/epsc2021-63
- 1189 Kahanpää, H., Newman, C., Moores, J., Zorzano, M.-P., Martín-Torres, J., Navarro,
 1190 S., ... Schmidt, W. (2016). Convective vortices and dust devils at the MSL
 1191 landing site: Annual variability. *Journal of Geophysical Research: Planets*,
 1192 121(8), 1514-1549. doi: 10.1002/2016JE005027
- 1193 Kahre, M. A., & Haberle, R. M. (2010). Mars co2 cycle: Effects of airborne dust and
 1194 polar cap ice emissivity. *Icarus*, 207(2), 648-653. doi: 10.1016/j.icarus.2009.12
 1195 .016
- 1196 Kahre, M. A., Murphy, J. R., Newman, C. E., Wilson, R. J., Cantor, B. A., Lem-
 1197 mon, M. T., & Wolff, M. J. (2017). The Mars dust cycle. In R. M. Haberle,
 1198 R. T. Clancy, F. Forget, M. D. Smith, & R. W. Zurek (Eds.), *The atmo-*
 1199 *sphere and climate of Mars* (p. 295–337). Cambridge University Press. doi:
 1200 10.1017/9781139060172.010
- 1201 Kieffer, H. H. (1979). Mars south polar spring and summer temperatures: A residual
 1202 co2 frost. *Journal of Geophysical Research: Solid Earth*, 84(B14), 8263-8288.
 1203 doi: 10.1029/JB084iB14p08263
- 1204 Kieffer, H. H., Neugebauer, G., Munch, G., Chase, S. C., & Miner, E. (1972). In-
 1205 frared thermal mapping experiment: The Viking Mars orbiter. *Icarus*, 16(1),
 1206 47-56.
- 1207 Kieffer, H. H., Titus, T. N., Mullins, K. F., & Christensen, P. R. (2000). Mars
 1208 south polar spring and summer behavior observed by TES: Seasonal cap evo-
 1209 lution controlled by frost grain size. *Journal of Geophysical Research: Planets*,
 1210 105(E4), 9653–9699. doi: 10.1029/1999je001136
- 1211 Lange, L., F.Forget, D.Banfield, M.Wolff, A.Spiga, E.Millour, ... W.B.Banerdt
 1212 (2022). *InSight Pressure Data Recalibration, and its Application to the*
 1213 *Study of Long-Term Pressure Changes on Mars*. Harvard Dataverse. doi:
 1214 10.7910/DVN/RUWICY
- 1215 Langevin, Y., Bibring, J.-P., Montmessin, F., Forget, F., Vincendon, M., Douté, S.,
 1216 ... Gondet, B. (2007). Observations of the south seasonal cap of Mars during

- 1217 recession in 2004–2006 by the OMEGA visible/near-infrared imaging spec-
 1218 trometer on board Mars Express. *Journal of Geophysical Research. Planets*,
 1219 *112*(E8), E08S12. doi: 10.1029/2006JE002841
- 1220 Leighton, R. B., & Murray, B. C. (1966). Behavior of carbon dioxide and other
 1221 volatiles on Mars. *Science*, *153*(3732), 136–144. doi: 10.1126/science.153.3732
 1222 .136
- 1223 Lemmon, M. T., Guzewich, S. D., McConnochie, T., de Vicente-Retortillo, A.,
 1224 Martínez, G., Smith, M. D., ... Jacob, S. (2019). Large dust aerosol sizes seen
 1225 during the 2018 martian global dust event by the curiosity rover. *Geophysical*
 1226 *Research Letters*, *46*(16), 9448-9456. doi: doi.org/10.1029/2019GL084407
- 1227 Malin, M. (2007). *Mro Mars color imager experiment data record level 0 v1.0*. NASA
 1228 Planetary Data System. doi: 10.17189/1520403
- 1229 Malin, M. C., Bell III, J. F., Calvin, W., Clancy, R. T., Haberle, R. M., James,
 1230 P. B., ... Caplinger, M. A. (2001). Mars color imager (marci) on the Mars
 1231 Climate Orbiter. *Journal of Geophysical Research E: Planets*, *106*(E8), 17651-
 1232 17672.
- 1233 Malin, M. C., Caplinger, M. A., & Davis, S. D. (2001). Observational evidence for
 1234 an active surface reservoir of solid carbon dioxide on Mars. *Science*, *294*(5549),
 1235 2146–2148. doi: 10.1126/science.1066416
- 1236 Martínez, G. M., Newman, C. N., De Vicente-Retortillo, A., Fischer, E., Renno,
 1237 N. O., Richardson, M. I., ... Vasavada, A. R. (2017). The Modern Near-
 1238 Surface Martian Climate: A Review of In-situ Meteorological Data from
 1239 Viking to Curiosity. , *212*(1-2), 295-338. doi: 10.1007/s11214-017-0360-x
- 1240 Martínez, G., Fischer, E., Rennó, N., Sebastián, E., Kempainen, O., Bridges, N.,
 1241 ... Gómez-Elvira, J. (2016). Likely frost events at gale crater: Analysis from
 1242 MSL/REMS measurements. *Icarus*, *280*, 93-102. (MicroMars to MegaMars)
 1243 doi: 10.1016/j.icarus.2015.12.004
- 1244 McCleese, D. J., Schofield, J. T., Taylor, F. W., Calcutt, S. B., Foote, M. C., Kass,
 1245 D. M., ... Zurek, R. W. (2007). Mars Climate Sounder: An investigation of
 1246 thermal and water vapor structure, dust and condensate distributions in the
 1247 atmosphere, and energy balance of the polar regions. *Journal of Geophysical*
 1248 *Research: Planets*, *112*(E5). doi: 10.1029/2006JE002790
- 1249 Millour, E., Forget, F., Spiga, A., Vals, M., Zakharov, V., Montabone, L., ... MCD
 1250 Development Team (2018). The Mars Climate Database (version 5.3). In *From*
 1251 *Mars Express to ExoMars* (p. 68).
- 1252 Mitchell, M. (1977). Evaluation of Viking lander barometric pressure sensor.
- 1253 Montabone, L., Forget, F., Millour, E., Wilson, R., Lewis, S., Cantor, B., ... Wolff,
 1254 M. (2015). Eight-year climatology of dust optical depth on Mars. *Icarus*, *251*,
 1255 65-95. (Dynamic Mars) doi: 10.1016/j.icarus.2014.12.034
- 1256 Montabone, L., Spiga, A., Kass, D. M., Kleinböhl, A., Forget, F., & Millour, E.
 1257 (2020). Martian year 34 column dust climatology from Mars Climate Sounder
 1258 observations: Reconstructed maps and model simulations. *Journal of Geophys-*
 1259 *ical Research: Planets*, *125*(8), e2019JE006111. doi: 10.1029/2019JE006111
- 1260 Moore, C. A., Moores, J. E., Newman, C. E., Lemmon, M. T., Guzewich, S. D., &
 1261 Battalio, M. (2019). Vertical and horizontal heterogeneity of atmospheric
 1262 dust loading in northern Gale crater, Mars. *Icarus*, *329*, 197-206. doi:
 1263 10.1016/j.icarus.2019.03.041
- 1264 Moores, J. E., Lemmon, M. T., Kahanpää, H., Rafkin, S. C., Francis, R., Pla-Garcia,
 1265 J., ... McCullough, E. (2015). Observational evidence of a suppressed plan-
 1266 etary boundary layer in northern gale crater, mars as seen by the navcam
 1267 instrument onboard the mars science laboratory rover. *Icarus*, *249*, 129-142.
 1268 (Special Issue: First Year of MSL) doi: 10.1016/j.icarus.2014.09.020
- 1269 Morris, E. C., & Jones, K. L. (1980). Viking 1 lander on the surface of mars: Re-
 1270 visited location. *Icarus*, *44*(1), 217-222.

- 1271 Newman, C. E., Kahanpää, H., Richardson, M. I., Martínez, G. M., Vicente-
 1272 Retortillo, A., & Lemmon, M. T. (2019). Marswrf convective vortex and
 1273 dust devil predictions for gale crater over 3 mars years and comparison with
 1274 msl-rems observations. *Journal of Geophysical Research: Planets*, *124*(12),
 1275 3442-3468. doi: 10.1029/2019JE006082
- 1276 Ordóñez-Etxeberria, I., Hueso, R., & Sánchez-Lavega, A. (2018, January). A
 1277 systematic search of sudden pressure drops on Gale crater during two Mar-
 1278 tian years derived from MSL/REMS data. , *299*, 308-330. doi: 10.1016/
 1279 j.icarus.2017.07.032
- 1280 Ordóñez-Etxeberria, I., Hueso, R., Sánchez-Lavega, A., Millour, E., & Forget,
 1281 F. (2019). Meteorological pressure at gale crater from a comparison of
 1282 REMS/MSL data and MCD modelling: Effect of dust storms. *Icarus*, *317*,
 1283 591-609. doi: 10.1016/j.icarus.2018.09.003
- 1284 Piqueux, S., & Christensen, P. R. (2008). Deposition of co2 and erosion of the
 1285 martian south perennial cap between 1972 and 2004: Implications for current
 1286 climate change. *Journal of Geophysical Research: Planets*, *113*(E2). doi:
 1287 10.1029/2007JE002969
- 1288 Piqueux, S., Kleinböhl, A., Hayne, P. O., Kass, D. M., Heavens, N., McCleese, D. J.,
 1289 ... Shirley, J. (2020). Atmospheric CO2 Depletion at the Surface in the Polar
 1290 Regions of Mars. In *Seventh international conference on mars polar science
 1291 and exploration* (Vol. 2099, p. 6016).
- 1292 Piqueux, S., Kleinböhl, A., Hayne, P. O., Kass, D. M., Schofield, J. T., & Mc-
 1293 Cleese, D. J. (2015). Variability of the martian seasonal co2 cap ext-
 1294 ent over eight Mars years. *Icarus*, *251*, 164-180. (Dynamic Mars) doi:
 1295 10.1016/j.icarus.2014.10.045
- 1296 Pla-Garcia, J., Rafkin, S. C., Kahre, M., Gomez-Elvira, J., Hamilton, V. E.,
 1297 Navarro, S., ... R. Vasavada, A. (2016). The meteorology of Gale crater
 1298 as determined from rover environmental monitoring station observations
 1299 and numerical modeling. part i: Comparison of model simulations with
 1300 observations. *Icarus*, *280*, 103-113. (MicroMars to MegaMars) doi:
 1301 10.1016/j.icarus.2016.03.013
- 1302 Pollack, J. B., Haberle, R. M., Schaeffer, J., & Lee, H. (1990). Simulations of the
 1303 general circulation of the martian atmosphere: 1. polar processes. *Journal of
 1304 Geophysical Research*, *95*(B2), 1447. doi: 10.1029/jb095ib02p01447
- 1305 Press, W. H., Teukolsky, S. A., Vetterling, W. T., & Flannery, B. P. (1993). *Nu-
 1306 merical recipes in FORTRAN; the art of scientific computing* (2nd ed.). USA:
 1307 Cambridge University Press.
- 1308 Rafkin, S. C., Pla-Garcia, J., Kahre, M., Gomez-Elvira, J., Hamilton, V. E., Marín,
 1309 M., ... Vasavada, A. (2016). The meteorology of Gale crater as determined
 1310 from rover environmental monitoring station observations and numerical mod-
 1311 eling. part ii: Interpretation. *Icarus*, *280*, 114-138. (MicroMars to MegaMars)
 1312 doi: 10.1016/j.icarus.2016.01.031
- 1313 Rangarajan, V. G., & Ghosh, M. (2020). Seasonal thermal inertia variations at Gale
 1314 crater: Role of active surface deposition phenomena. *Icarus*, *337*, 113499. doi:
 1315 10.1016/j.icarus.2019.113499
- 1316 Richardson, M. I., & Newman, C. E. (2018). On the relationship between sur-
 1317 face pressure, terrain elevation, and air temperature. part i: The large diur-
 1318 nal surface pressure range at gale crater, Mars and its origin due to lateral
 1319 hydrostatic adjustment. *Planetary and Space Science*, *164*, 132-157. doi:
 1320 10.1016/j.pss.2018.07.003
- 1321 Ryan, J. A., & Sharman, R. D. (1981). Two major dust storms, one mars year
 1322 apart: Comparison from Viking data. *Journal of Geophysical Research:
 1323 Oceans*, *86*(C4), 3247-3254. doi: 10.1029/JC086iC04p03247
- 1324 Seiff, A. (1976). The Viking atmosphere structure experiment - techniques, instru-
 1325 ments, and expected accuracies. *Space Science Instrumentation*, *2*, 381-423.

- 1326 Seiff, A., & Kirk, D. B. (1977). Structure of the atmosphere of Mars in summer at
 1327 mid-latitudes. *Journal of Geophysical Research*, *82*, 4364-4378. doi: 10.1029/
 1328 JS082i028p04364
- 1329 Spiga, A., Banfield, D., Teanby, N. A., Forget, F., Lucas, A., Kenda, B., ...
 1330 Banerdt, W. B. (2018). Atmospheric science with insight. *Space Science*
 1331 *Reviews*, *214*(7), 109. doi: 10.1007/s11214-018-0543-0
- 1332 Spiga, A., & Forget, F. (2009). A new model to simulate the martian mesoscale
 1333 and microscale atmospheric circulation: Validation and first results. *Journal of*
 1334 *Geophysical Research: Planets*, *114*(E2). doi: 10.1029/2008JE003242
- 1335 Spiga, A., Forget, F., Dolla, B., Vinatier, S., Melchiorri, R., Drossart, P., ...
 1336 Gondet, B. (2007). Remote sensing of surface pressure on Mars with the
 1337 Mars Express/OMEGA spectrometer: 2. meteorological maps. *Journal of*
 1338 *Geophysical Research: Planets*, *112*(E8). doi: 10.1029/2006JE002870
- 1339 Spiga, A., Murdoch, N., Lorenz, R., Forget, F., Newman, C., Rodriguez, S., ...
 1340 Banerdt, W. B. (2021). A study of daytime convective vortices and turbu-
 1341 lence in the martian planetary boundary layer based on half-a-year of insight
 1342 atmospheric measurements and large-eddy simulations. *Journal of Geophysical*
 1343 *Research: Planets*, *126*(1), e2020JE006511. doi: 10.1029/2020JE006511
- 1344 Steakley, K., & Murphy, J. (2016). A year of convective vortex activity at Gale
 1345 crater. *Icarus*, *278*, 180-193. doi: 10.1016/j.icarus.2016.06.010
- 1346 Streeter, P. M., Lewis, S. R., Patel, M. R., Holmes, J. A., Fedorova, A. A., Kass,
 1347 D. M., & Kleinböhl, A. (2021). Asymmetric impacts on Mars' polar vor-
 1348 tices from an equinoctial global dust storm. *Journal of Geophysical Research:*
 1349 *Planets*, *126*(5), e2020JE006774. doi: 10.1029/2020JE006774
- 1350 Taylor, P. A., Kahanpää, H., Weng, W., Akingunola, A., Cook, C., Daly, M., ...
 1351 Whiteway, J. (2010). On pressure measurement and seasonal pressure varia-
 1352 tions during the Phoenix mission. *Journal of Geophysical Research: Planets*,
 1353 *115*(E3). doi: 10.1029/2009JE003422
- 1354 Thomas, P., Calvin, W., Cantor, B., Haberle, R., James, P., & Lee, S. (2016). Mass
 1355 balance of Mars' residual south polar cap from CTX images and other data.
 1356 *Icarus*, *268*, 118-130. doi: 10.1016/j.icarus.2015.12.038
- 1357 Thomas, P., Calvin, W., Gierasch, P., Haberle, R., James, P., & Sholes, S. (2013).
 1358 Time scales of erosion and deposition recorded in the residual south po-
 1359 lar cap of Mars. *Icarus*, *225*(2), 923-932. (Mars Polar Science V) doi:
 1360 10.1016/j.icarus.2012.08.038
- 1361 Thomas, P., James, P., Calvin, W., Haberle, R., & Malin, M. (2009). Residual south
 1362 polar cap of Mars: Stratigraphy, history, and implications of recent changes.
 1363 *Icarus*, *203*(2), 352-375. doi: 10.1016/j.icarus.2009.05.014
- 1364 Tillman, J. (1989). *V1/v12 Mars meteorology resampled daily average pressure v1.0*.
 1365 NASA Planetary Data System. doi: 10.17189/ME53-8Z53
- 1366 Tillman, J. E. (1988). Mars global atmospheric oscillations: Annually synchron-
 1367 ized, transient normal-mode oscillations and the triggering of global dust
 1368 storms. *Journal of Geophysical Research: Atmospheres*, *93*(D8), 9433-9451.
 1369 doi: 10.1029/JD093iD08p09433
- 1370 Tillman, J. E., Johnson, N. C., Guttorp, P., & Percival, D. B. (1993). The mar-
 1371 tian annual atmospheric pressure cycle: Years without great dust storms.
 1372 *Journal of Geophysical Research: Planets*, *98*(E6), 10963-10971. doi:
 1373 10.1029/93JE01084
- 1374 Titus, T. N., Byrne, S., Colaprete, A., Forget, F., Michaels, T. I., & Prettyman,
 1375 T. H. (2017). The co2 cycle. In R. M. Haberle, R. T. Clancy, F. Forget,
 1376 M. D. Smith, & R. W. Zurek (Eds.), *The atmosphere and climate of Mars*
 1377 (p. 374-404). Cambridge University Press. doi: 10.1017/9781139060172.012
- 1378 Vicente-Retortillo, Á., Martínez, G. M., Renno, N., Newman, C. E., Ordóñez-
 1379 Etxeberria, I., Lemmon, M. T., ... Sánchez-Lavega, A. (2018). Seasonal
 1380 deposition and lifting of dust on Mars as observed by the Curiosity rover.

- 1381 *Scientific Reports*, 8(1). doi: 10.1038/s41598-018-35946-8
1382 Viúdez-Moreiras, D., Newman, C. E., de la Torre, M., Martínez, G., Guzewich, S.,
1383 Lemmon, M., . . . Gómez-Elvira, J. (2019). Effects of the my34/2018 global
1384 dust storm as measured by MSL REMS in gale crater. *Journal of Geophysical*
1385 *Research: Planets*, 124(7), 1899-1912. doi: 10.1029/2019JE005985
1386 Viúdez-Moreiras, D., Newman, C. E., Forget, F., Lemmon, M., Banfield, D., Spiga,
1387 A., . . . and, M. G. (2020). Effects of a large dust storm in the near-surface
1388 atmosphere as measured by InSight in elysium planitia, Mars. comparison
1389 with contemporaneous measurements by Mars science laboratory. *Journal of*
1390 *Geophysical Research: Planets*, 125(9). doi: 10.1029/2020je006493
1391 Withers, P. (2012). Empirical Estimates of Martian Surface Pressure in Support
1392 of the Landing of Mars Science Laboratory. , 170(1-4), 837-860. doi: 10.1007/
1393 s11214-012-9876-2
1394 Zhao, Y., Zhong, L., Yuan, R., Zhao, C., Li, R., Wang, Y., . . . Richardson, M.
1395 (2021). Simulation of martian dust effects on polar co2 ice caps and atmo-
1396 spheric circulation using the marswrf model. *Journal of Geophysical Research:*
1397 *Planets*, 126(12), e2021JE006937. (e2021JE006937 2021JE006937) doi:
1398 10.1029/2021JE006937

InSight Pressure Data Recalibration, and its Application to the study of Long-Term Pressure Changes on Mars

L.Lange¹, F.Forget¹, D.Banfield², M.Wolff³, A.Spiga^{1,4}, E.Millour¹, D.Viúdez-Moreira⁵, A.Bierjon¹, S.Piqueux⁶, C.Newman⁷, J.Pla-Garcia^{5,8}, W.B.Banerdt⁶

¹Laboratoire de Météorologie Dynamique, Institut Pierre-Simon Laplace (LMD/IPSL), Sorbonne Université, Centre National de la Recherche Scientifique (CNRS), École Polytechnique, École Normale Supérieure (ENS), Paris, France

²Cornell Center for Astrophysics and Planetary Science, Cornell University, Ithaca, NY, USA

³Space Science Institute, Boulder, CO, USA

⁴Institut Universitaire de France, Paris, France

⁵Centro de Astrobiología (CSIC-INTA) and National Institute for Aerospace Technology (INTA), Madrid, Spain

⁶Jet Propulsion Laboratory, California Institute of Technology, Pasadena, CA 91109, USA

⁷Aeolis Research, Unit 5, Chandler, AZ, USA

⁸Southwest Research Institute, Boulder, CO, USA

Contents of this file

Figures S1

Introduction

This document presents a figure illustrating the seasonal variations of MSL pressure measurements for the six martian years of the mission, after being interpolated to the Curiosity landing site.

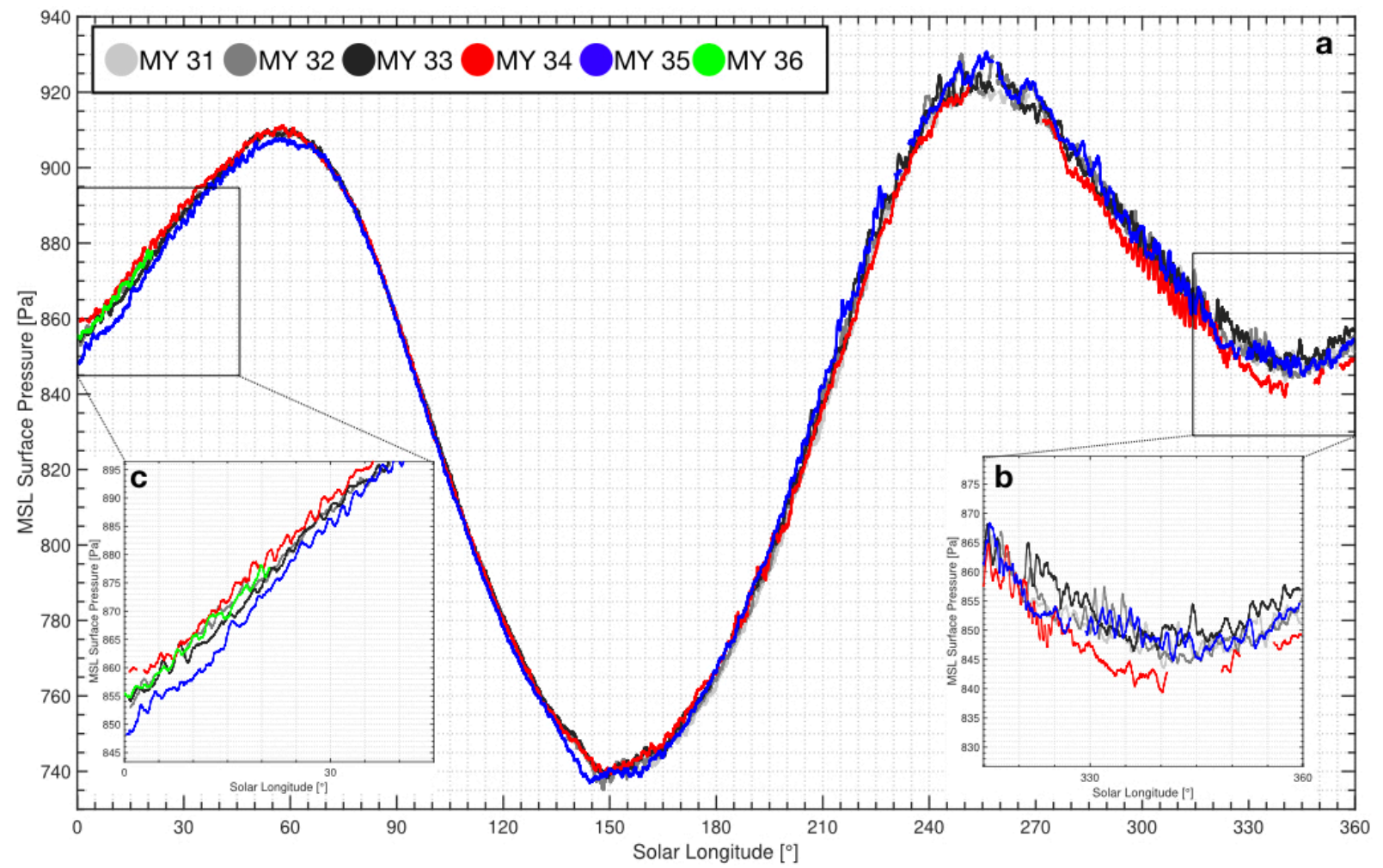


Figure S1. a: Diurnal averaged surface pressure recorded by MSL during the 6 martian years of the mission (light grey for MY 31, dark grey for MY 32, black for MY 33, red for MY 34, blue for MY 35, green for MY 36), after being interpolated to the MSL landing site to remove the influence of the rover's displacements. The interpolation method used is the one presented in section 2.2. b: Zoom on the pressure variations during the Northern Winter, between $315^\circ < L_s < 360^\circ$. c: Zoom on the pressure variations during the Northern Spring, between $0^\circ < L_s < 45^\circ$.